

Control and Dynamics of a Flexible Spacecraft during Stationkeeping Maneuvers

D. Liu and J. Yocum
Hughes Aircraft Company

D.S. Kang
C. S. Draper Laboratory

Summary

A case study of a spacecraft having flexible solar arrays is presented. A stationkeeping attitude control mode employing both earth and rate gyro reference signals and a flexible vehicle dynamics modelling and implementation is discussed.

The control system is designed to achieve both pointing accuracy and structural mode stability during stationkeeping maneuvers. Reduction of structural mode interactions over the entire mode duration is presented. The control mode employing a discrete-time observer structure is described to show the convergence of the spacecraft attitude transients during ΔV thrusting maneuvers without pre-loading thrusting bias to the on-board control processor. The simulation performance using the three-axis, body-stabilized nonlinear dynamics is provided.

The details of a five-body nonlinear dynamics model are discussed. The spacecraft is modelled as a central rigid body having cantilevered flexible antennas, a pair of flexible articulated solar arrays, and two gimbaled momentum wheels. The vehicle is free to undergo unrestricted rotations and translations relative to inertial space. A direct implementation of the equations of motion will be compared to an indirect implementation that uses a symbolic manipulation software to generate rigid body equations. A generalization of this approach to this class of flexible vehicles will be provided.

1. Introduction

Three-axis body stabilized spacecrafts having solar wings with significant structural flexibility may exhibit rigid-flex coupling effects during a typical stationkeeping maneuver. One of the primary concerns for the design of three-axis stabilized spacecraft is the structural mode interaction with the attitude control system. In addition, the dynamic analysis and the control performance evaluation are sensitive to the rigid-flex modelling accuracy. This paper presents a case study on the design, analysis and digital simulation of a microprocessor-based stationkeeping control system of a 3-panel communication spacecraft using thrusters as control actuators. It discusses the control system to achieve

modal stabilization, the dynamic model development and validation, and the technique for closed-loop digital simulation.

The vehicle under discussion is a three-axis stabilized geosynchronous communication satellite. The vehicle is powered by photovoltaic solar arrays and are controlled in its on-orbit operation by a combination of momentum wheels, reaction control thrusters, and solar array motion. This satellite is modelled as a central rigid body having cantilevered flexible antennas, a pair of flexible articulated solar arrays, and two gimbaled momentum wheels. The vehicle is free to undergo unrestricted rotations and translations relative to inertial space. The solar arrays rotate relative to the central body in response to the action of control torques. The momentum wheels are assumed to be controlled such that their motions relative to the central body are prescribed. In the deployed configuration, the solar arrays contain 75% of the total inertia of the satellite with only 7% of the total mass. Each solar array has 4 cantilevered frequencies below 1 Hz.

The solar wing flexibility is fully coupled into the body roll and yaw dynamics because the flexible solar wings are fixed about the roll and yaw axes of the central body, while articulating about its pitch axis. The pitch coupling depends upon the nonlinearity of the solar wing drive and its friction characteristics. The control bandwidth of the on-orbit normal mode is usually designed at a frequency well below the first structural mode so that the solar wing flexibility does not interact seriously with the normal mode controller. However, a relative high control bandwidth is needed to maintain pointing accuracy in the presence of a large thrusting disturbance. The disturbance torques are primarily induced by the offset of spacecraft center of gravity (CG) from the geometric or pressure center of maneuvering jets as well as the thrust mismatch. The sensed spacecraft flexible dynamics interact with the stationkeeping controllers, which may result in structural mode instability at high loop gains.

.During the thrusting maneuver, the dominant modes coupling in the stationkeeping control are phase stabilized using the lead inherent in the sensed gyro rates together with the phase-lead notch filters, while the non-dominant modes at higher frequencies are gain-stabilized. After the thrusting maneuver, any residual rates must be nulled by an order of magnitude in preparation for a smooth transfer back to the normal control mode. This paper will focus on the stationkeeping control during the thrusting maneuver only. The thrusting bias about each control axis is estimated such that a fast convergence on the bias estimates can be achieved without an open-loop torque pre-bias by ground command, although this feature is also included in the design. The control loop bandwidths are designed as high as possible to meet pointing requirements, while still achieving adequate modal stability. Simulation results demonstrate stationkeeping control performance from a typical 2-jet (5 lbf each) south maneuver under the worst case maneuvering conditions are presented.

To verify the accuracy of the dynamics model, two approaches are taken. In the first approach, the direct approach, the equations of motion for the vehicle are derived from fundamental momentum principles. The flexible appendages are modelled with conventional lumped mass model employing stiffness matrices to characterize the internal energy. Transformations to appendage modal coordinates are made and a reduction in the number of elastic degrees of freedom is achieved through their truncation. Simplifying assumptions are made regarding the magnitude of certain nonlinear kinematic terms based on operational considerations. The final set of governing equations are coded in a first order form suitable for numerical integration.

In the second approach, the indirect approach, an unconventional method is employed. The "rigid" portion of the equations and the code is obtained from a symbolic

manipulation software. The "rigid/flex" coupling terms are derived and implemented. The details of this approach will be presented later in this paper. The two approaches were numerically compared through a set of chosen open loop comparison tests.

2. Performance Requirements and Control System Descriptions

Performance Requirements

The spacecraft under study requires at least 400 bi-weekly south maneuvers with a maximum duration of 120 sec per maneuver using two 5 lbf thrusters. East/west corrections are 5 sec short burn each. Factors affecting pointing accuracy during the stationkeeping maneuver are earth sensor noise, rate gyro noise, gyro rate bias estimation errors, thrusters pulse-to-pulse repeatability, spacecraft CG offset, CG migration due to propellant motion, flexibility of solar wings and reflectors, thrust mismatch, thruster misalignment, on-time/off-time thruster delay, thruster plume-impingement, etc. Effects due to environment disturbance such as solar torques, magnetic torques, wing torques, etc., are assumed to be negligible. The goal is to maintain body transients to within ± 0.1 deg in roll/pitch and ± 0.2 deg in yaw. The control loops should stabilize structural mode oscillation seen on spacecraft attitude and provide stability range in the presence of structural mode frequency uncertainty.

Control Algorithms

The stationkeeping control is executed through special control algorithms that run when the spacecraft is in Stationkeeping Mode. Due to the spacecraft CG offset and variation in thrust pulse amplitude, various thrusting disturbance torques about the control axes may be induced when the maneuver thrusters are activated. Stationkeeping Mode provides thruster control for a maneuver execution and autonomous attitude control to limit body transient errors and maintain pointing accuracy during maneuvers. Attitude control in roll and pitch axes is achieved using earth referenced signals and rate integrating gyro data with 5 lbf thrusters. A rate integrating gyro is used as rate references in yaw control.

Figure 2.1 shows the functional block diagram of the 3-axis stationkeeping attitude control system during maneuvers. The control logic for each of roll and pitch rate loops in Stationkeeping Mode is combined with the gyro referenced attitude estimator for position, rate and acceleration bias estimates and the proportional controller for control acceleration command generation. Using earth referenced pitch and roll position signals, effects due to gyro drift can be minimized by an on-board software calibration to the raw rate measurements. The yaw control logic in Stationkeeping Mode is identical to the roll and pitch channels except for the yaw gyro bias estimate, which is constant based on premaneuver calibration estimate. The technique for rate gyro calibration will not be discussed in this paper.

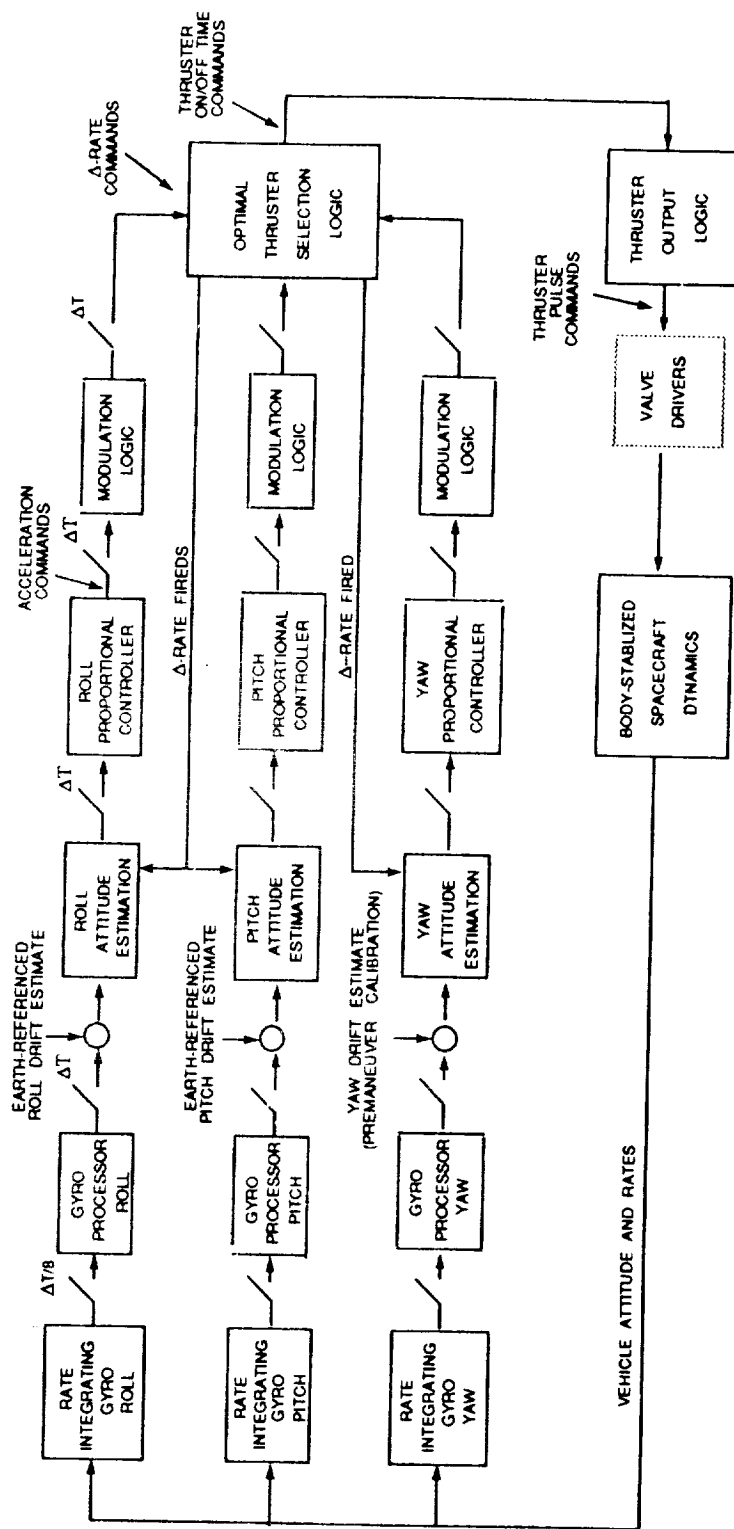


Figure 2.1 Functional Control Block Diagram of Stationkeeping Mode

The earth referenced pitch and roll position errors are sensed at 2.0345 Hz, i.e. every 30 real time interrupts (RTIs) at 16.384 msec per RTI, to supply position references for the roll and pitch gyro calibration. The angle estimate is obtained by adding the gyro bias estimate to the raw rate measurement, and integrating the resulting rate. For the yaw control loop, it does not perform the yaw gyro calibration during maneuver, since no yaw position references are available in Stationkeeping Mode. Instead, yaw gyro bias is estimated in the normal mode prior to maneuver, and its value is held throughout the maneuver.

The gyro referenced rate measurements with calibration are sensed every 8 RTIs to supply rate references to a third-order attitude estimator for each axis. Each attitude estimator performs two functions. First, it integrates the gyro rate (after correction for bias) to obtain a position estimate. Both the roll and pitch gyro calibration along with integrations operate during the premaneuver gyro calibration period as well as throughout the maneuver. Second, it estimates the spacecraft angular rate and acceleration bias about the respective axis. The roll and yaw attitude estimators also include the effect of roll-yaw coupling due to spinning wheel momentum.

A proportional controller is employed for each axis to determine the control acceleration commands based upon the position, rate and acceleration bias estimates. The control acceleration commands are held constant over each control sample period. The on-board optimal thruster selection (OTS) logic selects available thrusters and determines necessary thruster on/off command duration to valve drivers based upon the minimum fuel consumption. The selected 5 lbf thrusters are turned on/off for commanded durations to deliver the control momentum equivalent to the commands, and achieve attitude corrections during maneuvers. The detailed technique for conversion of the control acceleration commands to thruster commands will not be discussed further. Although the control sample period is designed to be commandable, it must be selected to meet the needs of the control processor thruput and avoid structural mode instabilities as well.

3. Flexible Spacecraft Model Descriptions

The mechanical idealization of the satellite is illustrated in Figure 3.1. The model consists of a central body, which is considered to be rigid and to which are mounted a set of reaction control thrusters. Cantilevered to the central body are a complement of structurally flexible antennas. Two distinct, structurally flexible solar arrays are hinge connected to the central body. The arrays can rotate independently about parallel drive axes in response to control torques, which are assumed to be known functions of time. Two independent, identical, rigid axisymmetric, variable-speed momentum wheels are mounted to the central body through two-axis gimbal mechanisms. The complete motions of the wheels relative to the central body are assumed to be prescribed functions of time.

The communications antennas of the actual satellite are capable of limited articulation relative to the central body. However, because these rotations are small in both magnitude and rate, their influence on the vehicle's overall attitude dynamics was deemed negligible, and these degrees of freedom were not included in the model. While the solar arrays will be virtually identical under nominal circumstances, they are treated as structurally distinct to accommodate more general conditions.

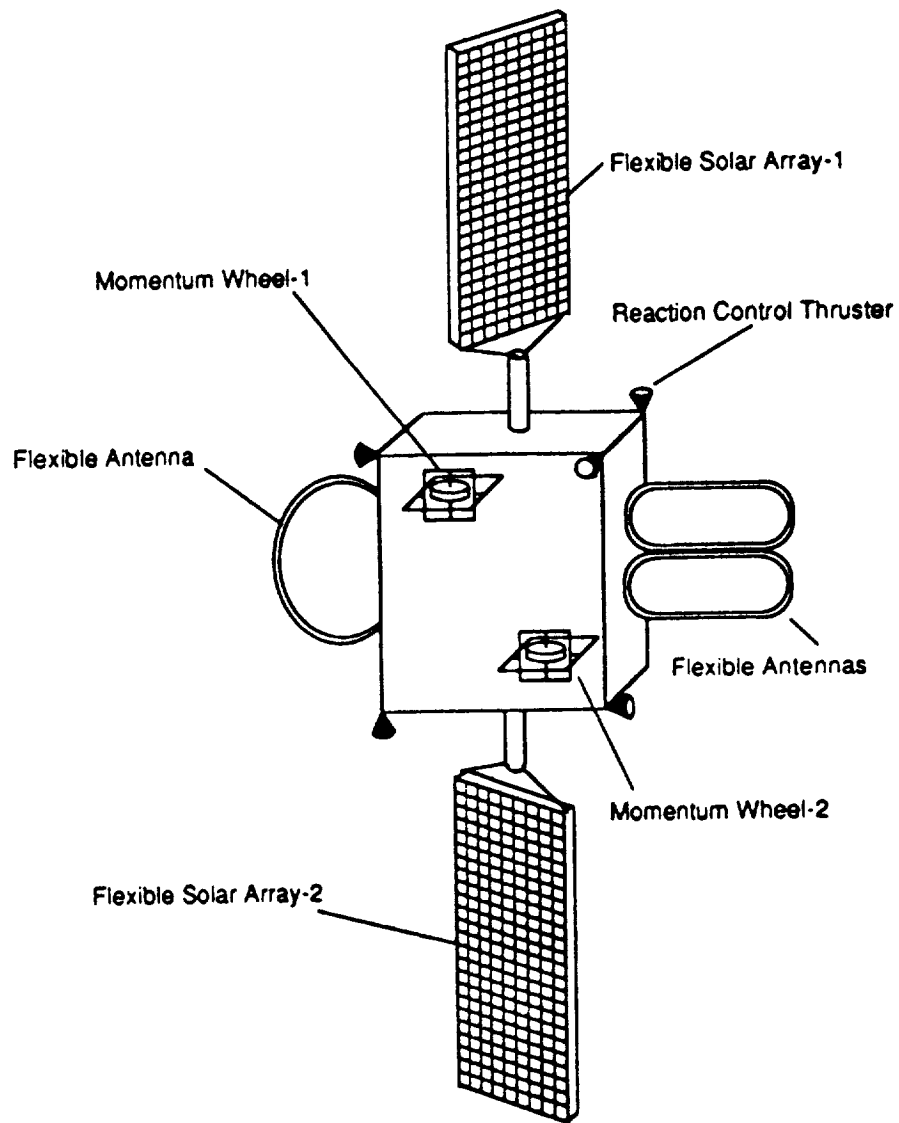


Figure 3.1. Mechanical Idealization of a satellite.

The deformations of the antenna and solar array structures are assumed to be linear elastic in character and small in magnitude. The respective appendages are modelled as collections of point masses interconnected by massless elastic structure. Stiffness matrices are used to define the elastic restoring forces acting internal to these assemblies. Ultimately, modal coordinate transformations are introduced for each appendage and the final motion equations are cast in terms of truncated sets of those variables.

Cantilevered frequencies of an individual solar array and of an assembled antennas are provided in Table 3.1.

Table 3.1. Characteristic Cantilevered Frequencies of the Appendages.

Mode #	Solar Array Frequency (Hz)	Antennas Frequency (Hz)
1	.118	1.586
2	.355	1.792
3	.705	1.953
4	.835	2.043
5	1.825	4.235
6	2.725	4.867
7	3.167	5.323
8	4.914	5.893
9	6.161	13.366
10	6.905	19.558

4. Control Design and Analysis

Linearized Spacecraft Open Loop Dynamics

Let $\{b\}$ be the spacecraft body frame, $\{s\}_w$ be the solar wing frame and C_w be the direction cosine matrix at the wing-to-body angle α such that $\{s\}_w = C_w\{b\}$, where $w = n$ (North wing) or s (South wing). Figure 4.1 is a geometry showing the spacecraft with the thrusting forces and torques and the disturbance created by thruster plume impingement; in which we assume that point i is the pressure center on North wing where the resultant plume force vector applies.

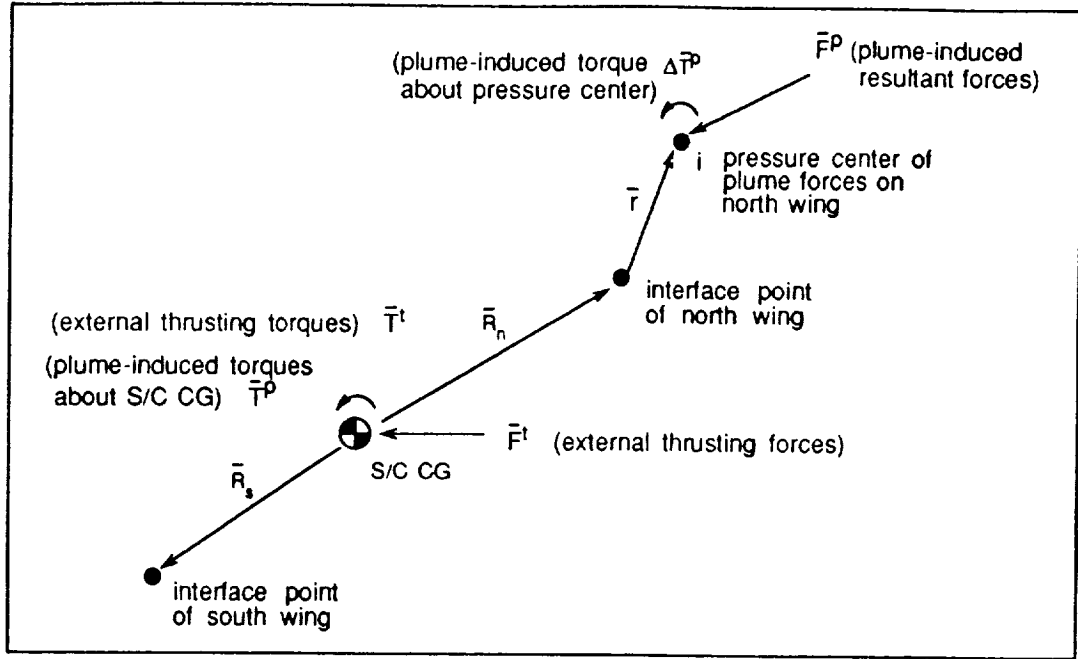


Figure 4.1 A Geometry showing External Thrusting Forces/Torques and Plume Disturbance

The linearized body-stabilized spacecraft hybrid dynamics with articulated solar wings are given in Equations (4.1) - (4.6).

$$m \ddot{x} + P_n \eta_n + P_s \eta_s = F^t + F^P \quad (\text{S/C translational motion}) \quad (4.1)$$

$$I_{s/c} \dot{\omega} + I_n e_2 \dot{\omega}_n + I_s e_2 \dot{\omega}_s + Q_n \ddot{\eta}_n + Q_s \ddot{\eta}_s = T^t + T^P \quad (\text{S/C rotational motion}) \quad (4.2)$$

$$e_2^T I_n \dot{\omega} + I_n^m \dot{\omega}_n + e_2^T Q_n^o \ddot{\eta}_n = T_n^{swd} \quad (\text{North wing pitch dynamics}) \quad (4.3)$$

$$e_2^T I_s \dot{\omega} + I_s^m \dot{\omega}_s + e_2^T Q_s^o \ddot{\eta}_s = T_s^{swd} \quad (\text{South wing pitch dynamics}) \quad (4.4)$$

$$P_n^T \ddot{x} + Q_n^T \dot{\omega} + (e_2^T Q_n^0)^T \dot{\omega}_n + \ddot{\eta}_n + 2\zeta\Lambda \dot{\eta}_n + \Lambda^2 \eta_n = \Phi_i^T \begin{bmatrix} C_n FP \\ \Delta T_i^p \end{bmatrix} \quad \text{(North wing flex dyn.)} \quad (4.5)$$

$$P_s^T \ddot{x} + Q_s^T \dot{\omega} + (e_2^T Q_s^0)^T \dot{\omega}_s + \ddot{\eta}_s + 2\zeta\Lambda \dot{\eta}_s + \Lambda^2 \eta_s = 0 \quad \text{(South wing flex dyn.)} \quad (4.6)$$

where

- m = total S/C mass
- $I_{s/c}$ = S/C mass inertias
- x = S/C translational position vector
- ω = S/C angular rate vector
- I_n, I_s = pitch inertias of wings about their interface points
- ω_n, ω_s = relative pitch angular rates of wings
- η_n, η_s = modal variables of wings
- P_n^0, P_s^0 = rigid-flex translational coupling matrices of wings about their interface points
- P_n, P_s = rigid-flex translational coupling matrices of wings about the S/C CG
- Q_n^0, Q_s^0 = rigid-flex rotational coupling matrices of wings about their interface points
- Q_n, Q_s = rigid-flex rotational coupling matrices of wings about the S/C CG
- T_n^{swd}, T_s^{swd} = solar wing torques
- $FP, \Delta TP$ = plume induced force and torque about pressure center
- Φ = mode shape at point i of North wing (a nx6 matrix with 3 translational and 3 rotational deformation, where n is the number of modes in concern)
- Λ = cantilever mode frequencies for each wing
- ζ = structural damping factor
- e_2 = $[0 \ 1 \ 0]^T$

The model above is with articulated solar wings driven by the wing torques about their hinge axes. To fully include the flexibility of wings, the dynamic inertias of each wing referenced to its interface point must contain at least 99% of the roll or yaw moment of inertia about the same point, or, the pitch inertia excluding yoke. The flexible reflectors have relatively small dynamic inertias compared to the total spacecraft mass inertias; the structural mode control interaction is negligible. Therefore, the reflectors are considered to be rigid and included as a part of rigid central body in stability analysis. For the pitch dynamics of wings in the "constraint" state (see Design Considerations below for further discussion), the solar wing angular acceleration terms in Equations (4.1), (4.2), (4.4) and (4.5) may be eliminated from these equations, and the resulting model represents the linearized spacecraft dynamics with non-articulated wings.

Control Design Model of Rate Loops

The control system has an outer loop (i.e. position loop) and an inner loop (i.e. rate loop). The position loop is designed at very low bandwidth with its gain crossover well below the structural modes and consequently has generous gain margin (> 40 dB) on all flexible modes. As for the modal stability, the rate loops are the primary concerns. The design model of rate control loops in Stationkeeping Mode is given below.

$$\text{Rate Gyro Dynamics} \quad \theta_i^g = \frac{1}{s} \frac{a_g}{s + a_g} \omega_i \quad (i=1,2,3)$$

$$\text{Gyro Processors} \quad \omega_i^g(n+1) = [\theta_i^g(n+1) - \theta_i^g(n)] / \Delta T$$

$$\text{Attitude Estimators} \quad \hat{\theta}_i^g(n+1) = \hat{\theta}_i^g(n) + \Delta T \omega_i^g(n+1)$$

$$\bar{\omega}_i^g(n+1) = \hat{\omega}_i^g(n) + \Delta \omega_i^l(n) + \Delta T \hat{d}_i(n) + \Delta \omega_i^c(n)$$

$$\hat{\omega}_i^g(n+1) = \bar{\omega}_i^g(n+1) + K_r [\omega_i^g(n+1) - \bar{\omega}_i^g(n+1)]$$

$$\hat{d}_i(n+1) = \hat{d}_i(n) + K_d [\omega_i^g(n+1) - \bar{\omega}_i^g(n+1)]$$

$$\Delta \omega_i^c(n) = -(H_T \Delta T / I_1) \hat{\omega}_3^g(n) \quad (i=1)$$

$$= 0 \quad (i=2)$$

$$= (H_T \Delta T / I_3) \hat{\omega}_1^g(n) \quad (i=3)$$

$$\Delta \omega_i^l(n) = \Delta T \alpha_i^{pf}(n-1)$$

$$\text{Proportional Controllers} \quad \alpha_i^{pf}(z) = -N_p(z) \left(C_p \hat{\theta}_i^g + C_r \hat{\omega}_i^g \right) - \hat{d}_i(z)$$

$$N_p(z) = \frac{n_2 z^2 + n_1 z + n_0}{z^2 + d_1 z + d_0} \quad (\text{Phase Lead Notch Filter})$$

Control Transport Delay

$$\alpha_i^T = \frac{\Delta T}{\tau_c} \alpha_i^{pf}(n-\mu) \quad \text{if } n \Delta T + \tau_d \leq t \leq n \Delta T + \tau_d + \tau_c, \mu = (\tau_d + .5 \tau_c) / \Delta T$$

$$= 0 \quad \text{otherwise}$$

where

$$\theta_i = \text{spacecraft angular position about body axis } i \text{ [deg]}$$

$$\omega_i = \text{spacecraft angular rate about body axis } i \text{ [deg/sec]}$$

$$\hat{\theta}_i^g = \text{estimate of } \theta_i \text{ [deg]}$$

ω_i^g	=	rate gyro measurement with calibration [deg/sec]
$\hat{\omega}_i^g$	=	estimate of ω_i [deg/sec]
\hat{d}_i	=	acceleration bias estimate about body axis i [deg/sec ²]
θ_i^g	=	position signal output from the rate integration gyro [deg]
RTI	=	real time interrupt = 16.384 msec
α_i^{pf}	=	filtered control acceleration commands
α_i^T	=	actual control acceleration acting about body axis i over τ_c [deg/sec ²]
$\Delta\omega_i^f$	=	feedforward rate changes [deg/sec]
ΔT	=	control sample period [sec]
τ_d	=	control pulsing delay [sec]
τ_c	=	actual control pulsewidth [sec]
n	=	control sampling time in Stationkeeping Mode
K_r	=	rate estimation gain [(deg/sec)/(deg/sec)]
K_d	=	acceleration bias estimation gain [(deg/sec ²)/(deg/sec)]
C_p	=	spacecraft position control gain in Stationkeeping Mode [sec ⁻²]
C_r	=	spacecraft rate control gain in Stationkeeping Mode [sec ⁻¹]
$N_p(z)$	=	phase-lead notch filter, $z=e^{s\Delta T}$
a_g	=	gyro servo bandwidth [rad/sec]
I_i	=	spacecraft moment of inertias about body axis i [slug-ft ²]
H_T	=	total spacecraft angular momentum about pitch axis

It employs a discrete predictor-corrector algorithm to estimate the spacecraft rate and acceleration bias and the integration of the rate measurement (after correction for gyro bias) for position estimate. A discrete phase-lead notch filter is added in series with the attitude control acceleration command (i.e. the proportional controller excluding the acceleration bias control term, which is added to the filtered attitude control acceleration command) to provide additional phase lead for modal stabilization. The spacecraft dynamics used in the design are represented by the linearized hybrid dynamic model. The rate gyro model, which has a first order servo of 8 Hz bandwidth, output positional signal, and the gyro processor determines the rate based upon the position change over one control sample period. The equivalent transfer function of the design model will not be given in this paper. We will discuss various design concerns which are related to transient performance and structural mode stability in general, and the design philosophy in achieving the goals.

Sensitivity To Modal Parameters

The stability of the structural modes selected for baseline design may be affected by both the structural frequency uncertainty and the structural damping. A structural damping ratio of 0.0025-0.005 is added to the hybrid dynamic model. The P and Q matrices defined earlier are essentially the diagonal matrix elements of the translational and rotational rigid-flex coupling matrix B given in Equation (6.9). The coupling matrix selected for the baseline design is derived based upon the the spacecraft on orbit nominal configuration with fully deployed wings whose z-axis is directed to the Earth. By knowing the location of the interface point relative to the spacecraft CG and the wing orientation, it can be proved

that conversion of the coupling parameters to about the spacecraft CG is accomplished through the relations:

$$P_n = C_n^T P_n^0, \quad Q_n = C_n^T Q_n^0 + \tilde{R}_n P_n \quad (4.7)$$

$$P_s = C_s^T P_s^0, \quad Q_s = C_s^T Q_s^0 + \tilde{R}_s P_s \quad (4.8)$$

where "~" denotes the skew symmetric matrix operator which achieves a vector cross product. P and Q will change when the spacecraft is no longer in nominal configuration under the following two conditions. First, P and Q vary as the wings rotate about their hinge axes; and second, due to the nonlinear characteristics of panel hinge stiffness. The solar wings could be at any orientation with 16 deg or less wing separation angle. Rotation of wings will primarily affect P and Q about the spacecraft body roll and pitch axes, and almost no change about the body pitch axis in the presence of the symmetric north/south wings. Furthermore, when the east or west thrusters fire during an east/west maneuver with non-zero wing angles, the panel hinge loads as induced primarily by the linear acceleration of the spacecraft along the the panel z-axis as well as the flexibility of wings may exceed the spring preload such that the panel stiffness will drop from its hardstop region, where the nominal P and Q are derived, to the deadband region, where a soft panel stiffness is present. The worst case panel hinge loads result when the wing is at 90 deg orientation during an east/west maneuver. When this occurs, P^0 and Q^0 about the interface point of the wing will vary about all three axes. Both the roll and yaw control axes must be designed to stabilize all possible structural mode frequencies which may result from the rotation of wings and the nonlinear characteristics of panel stiffness.

Spacecraft CG Uncertainty

The CG offset of the spacecraft from the pressure center of maneuver thrusters will result in a thrusting disturbance about the control axis. If the actual CG offset was predicted to a 100% accuracy by the OTS in advance, the thrusting disturbance would be self-compensated with the selected thrusters -- the unique feature of the OTS. The CG uncertainty of the spacecraft has a major impact on the maneuver transients. The concerns are in two areas: (i) the CG uncertainty of the spacecraft while on station at a steady state condition, which is primarily caused by the tank misalignment and the possible imbalance of the dry spacecraft and (ii) the CG uncertainty due to propellant motion during a maneuver. The estimation errors on the acceleration bias may result in an initial transient about each axis that exceeds steady state pointing. The acceleration bias estimation gain (K_d) must be designed to minimize the maneuver initialization transient, and to avoid excitation of structural modes, while still being able to track disturbance. The transient errors can also be improved with an initialization of the acceleration bias estimates to the steady state values recorded from the last maneuver.

Firing Thrusters on Flexure

The wing flexibility may be fully excited in the steady state condition from a long maneuver burn. Also, when switching the control logic to further null the rigid body residual rates at the completion of a maneuver, an instant loss of thrusting forces could yield a significant response to the already excited flexible dynamics with the magnitude exceeding the impulse control deadband limits. To avoid firing on flexure, the rate

estimation gain (K_r) in Stationkeeping Mode must be as low as possible to filter the sensed spacecraft flexible dynamics, so that the proportional controllers determine the required control momentum based upon the estimated rigid body dynamics. The rate gain in the range $0 < K_r < 0.5$ (deg/sec)/(deg/sec) meet the requirement, while still being able to track the spacecraft dynamics to a degree of accuracy by feeding forward the commanded rate changes to the estimators from the OTS.

Control Transport Delay

Due to onboard control software processor speed, a computational delay on rate change command processing in OTS is induced. Such a delay together with the phase delay induced by the gyro rate signal processing and the control pulsewidth delivery induce a phase lag to each control loop, which affects the stability of structural modes. To compensate for the loss of phase due to the control transport delay, a phase-lead notch filter is employed in Stationkeeping Mode to provide each control loop with an additional phase lead. The design philosophy is to set the modulation frequency so that the half sample frequency is well above the dominant modes to ensure phase stabilization of these modes with additional phase lead produced by the notch filter. Because the notch filter is not wide enough to provide all modes with sufficient phase lead, the modes near the half sample rate are gain-stabilized. Phase stabilization of the dominant modes simply means that the control loop will generate a stabilizing feedback signal to that mode. This is to be contrasted to gain stabilization wherein the non-dominant modes rely upon the structural damping of the spacecraft to provide enough damping to overcome any slight destabilizing effects.

Effect of SWD Deadband on Torsional Mode Stability

Due to the solar wing drive (SWD) backlash, the flexible pitch dynamics of wings about their interface points may appear in one of the three states: "free-free", "constraint" and one between these two states, depending upon whether the wings are inside or outside the deadband and the magnitude of friction. The SWD has a 0.5° deadband. When the wings are inside the deadband and the magnitude of friction is insufficient to overcome the wing relative motion, the central body pitch dynamics are then disturbed by the load torques with a phase-shifted bang-bang profile whose magnitude is equal to Coulomb friction. It is very complex to analyze the torsional mode stability with such a profile. The best way to examine the performance is through the simulation by actually including the SWD. When the wings are inside the deadband but the friction is negligible so that the flexible dynamics of each wing are "free-free" about its pitch axis, the central body pitch dynamics are then fully decoupled from the wing relative motion. The central body under this state is considered to be rigid. The stabilities of the "free-free" modes will not become a problem as long as the free-free motion remains inside the deadband. Still, when inside the deadband but the relative motion of the wing is locked up by friction, or, the wing-to-body rates are large enough to break the friction and the gear teeth are recontacted to the SWD shaft, the pitch flexible dynamics of wing are now considered to be "constrained" about its pitch axis; that is, the SWD will output load torques in absence of stepping commands, to drive the wings to prevent them from moving about the pitch axis of the central body. From this viewpoint, the wings are also fixed to the central body about its pitch axis and the flexible dynamics of wings are fully coupled into the body pitch axis through the load torques.

Plume Impingement Effects

Forces and torques created by thruster plume impingement on spacecraft appendages (north wing and east/west antennas) may result in a net change in the overall control torques and an unmodelled excitation of the structural modes. From the spacecraft stability viewpoint, the principle concern is that the plume disturbance shall not add phases to erode the phase margins of the phase stabilization modes nor magnify amplitudes to degrade the gain margins of the gain stabilization modes.

Since \bar{r} is the pressure center of plume forces, the plume induced torques about the deformed S/C CG is

$$\bar{T}^P = (\bar{R}_n + \bar{r}) \times \bar{F}^P + \Delta \bar{T}^P$$

$$\Delta \bar{T}^P = \bar{T}^P - (\bar{R}_n + \bar{r}) \times \bar{F}^P = \{s\}^T \{C_n T^P - (\bar{C}_n \bar{R}_n + \bar{r})(C_n F^P)\}$$

or

$$\Delta T^P = C_n T^P - (\bar{C}_n \bar{R}_n + \bar{r})(C_n F^P)$$

Referring to Equation (4.5), the modal excitation of the north wing is induced by (i) the spacecraft and the north wing motion driven by the terms

$$\epsilon_n = P_n^T \ddot{x} + Q_n^T \dot{\omega} + (e_2^T Q_n^T)^T \dot{\omega}_n$$

and (ii) the plume disturbance

$$\epsilon^P = \Phi^T [(C_n F^P)^T (\Delta T^P)^T]^T$$

acting about point i, the assumed pressure center of plume forces.

In the presence of the plume disturbance ϵ^P acting on the North wing, the open loop dynamics transfer function $\omega(s)/T^i(s)$ from an impulse response can be derived from the single axis hybrid dynamic model with one mode only as

$$\frac{\omega(s)}{T^i(s)} = \frac{1}{I_{s/c}} \frac{1-\mu_1}{1-\mu_2} \frac{s^2 + 2\zeta_1\lambda_1 s + \lambda_1^2}{s^2 + 2\zeta_2\lambda_2 s + \lambda_2^2} \frac{1}{s}$$

where

$$\mu_1 = \epsilon^P q_n / T^i$$

$$\mu_2 = 2 q_n^2 / I_{s/c}$$

$$\zeta_1 = \zeta / \sqrt{1-\mu_1}$$

$$\zeta_2 = \zeta / \sqrt{1-\mu_2}$$

$$\lambda_1 = \lambda / \sqrt{1-\mu_1}$$

$$\lambda_2 = \lambda / \sqrt{1-\mu_2}$$

The parameters ϵ^P and q_n are the plume disturbance and the rigid-flex rotational coupling term associated with the structural mode of frequency λ and modal damping ζ . T^* is the impulse thrusting torque about the single axis in concern. If $\mu_1 \neq 0$ (i.e. $\epsilon^P \neq 0$), the plume disturbance will perturb the zeros of the transfer function above from their nominal locations. If the perturbed zeros move toward the poles (i.e. $\mu_1 > 0$), then it improves the margin of the phase-stabilized mode, producing less rigid-flex coupling. On the contrary, if $\mu_1 < 0$, the zeros move away from the poles, and the loop gain is magnified by a factor of $(1 - \mu_1)$: both of these factors will erode the margin of any gain-stabilized mode.

The geometry of the thrusters and solar wings are such that, in fundamental modes (those with no inflection points), the plume impingement coupling and the rigid-flex dynamic coupling act in phase with one another to excite a mode. In other words, plume impingement acts to amplify modal excitation already present due to rigid-flex dynamic coupling. This implies that $\mu_1 < 0$ for fundamental modes. In this case, the zeros of the transfer function move even further from the poles, exacerbating the flexible dynamics coupling problem for these modes. Thus if $\mu_1 < 0$, it is desirable to have the magnitude of μ_1 as small as possible: $|\mu_1| \ll |\mu_2|$ is goodness. In this case study, $\mu_1 = -0.0388$ for the first out-of-plane mode at 0.1185 Hz. Fortunately, values are small in comparison to the corresponding $\mu_2 = 0.7037$, indicating that plume impingement is not a dominant effect. One measure is the zero/pole frequency ratio: with no plume impingement

$$\frac{\lambda_1}{\lambda_2} = \sqrt{1 - \mu_2} = \sqrt{1 - 0.7037} = .544$$

whereas with plume impingement

$$\frac{\lambda_1}{\lambda_2} = \sqrt{\frac{1 - \mu_2}{1 - \mu_1}} = \sqrt{\frac{1 - 0.7037}{1 + 0.0388}} = .534$$

This is a change of only 1.87% which is small relative to the 5% or 10% accuracy to which μ_2 is known to begin with (A 1.58% change in the value of μ_2 would result in the same change in zero/pole ratio).

Higher frequency modes whose mode shapes include an odd number of inflection points between the attach point and the "point of application" of the plume impingement force can exhibit a positive value for μ_1 . In this case, the plume impingement force acts opposite to the direct rigid-flex dynamic coupling and tends to reduce modal excitation. In the transfer function this is reflected by the fact that the zeros move closer to the poles, thus tending to cancel. Should μ_1 ever get as big as μ_2 , the zero would exactly cancel. An even higher value of μ_1 would reverse the phase of the modal coupling. This situation is of less interest, and is probably not possible with plume impingement as the excitation source. Since plume impingement is, in reality, a distributed force rather than a point force as modeled herein, its viability in exciting a higher frequency mode diminishes rapidly as the

number of inflection points increases. The assumption made herein that plume impingement force is applied at a single point loses its validity for higher frequency modes, therefore results should not be taken too literally for such modes. The "constrained" state is similar to those for roll or yaw loop.

5. Control Loop Stability

With the panel support cantilevered at its base about the transverse axes, but free in torsion, Table 5.1 characterizes the flexibility of 0 deg, 3-panel single wing in terms of the modal frequencies with associated dynamic inertias about the interface point of wing. The first twelve modes as listed contain > 99% of the total inertias of wing about each axis, which are sufficient to describe the flexible characteristics of wings. When the wings are attached to their base, the flexible dynamics appeared to the angular motion of the spacecraft through rigid-flex coupling have frequencies higher than that of the cantilever modes. The increased modal frequencies, assuming perfectly symmetric wings, are defined as the system modes in Table 5.1. The frequencies of the system modes will shift as the wings rotate about the hinge axes; 90 deg wings yield out-of-plane cantilever modes in the yaw axis and in-plane cantilever modes in the roll axis. For the transfer function of the corresponding open loop dynamics, the dominant modes have wider pole/zero separations. One of the design goals is to stabilize the system modes under any wing orientation.

Mode	Frequency, Hz			Dynamic Inertia (about interface point), Kg-m ²	Definition
	Cantilever	System			
		Constraint	Free-Free		
1	0.1185	0.2117	1.3645	44.498	out-of-plane
2	0.3547	0.6323		45.970	in-plane
3	0.7051	0.7631		8.722	out-of-plane
4	0.8508	0.8582		4.498	torsional
5	1.8254	1.8627	3.1938	3.550	out-of-plane
6	2.8058	2.8091		1.588	torsional
7	3.1668	3.2573		3.412	out-of-plane
8	5.1320	5.1338	5.3698	0.854	torsional
9	6.1608	6.1704	9.1631	0.592	out-of-plane
10	8.2235	8.2333		0.432	out-of-plane
11	8.9668	8.9898		0.643	torsional
12	9.4732	9.4882		9.7306	0.524

Figure 5.1 shows the discrete-time Bode plots and Nichols chart of the 8*RTI Stationkeeping Mode spacecraft roll rate control loop with no structural filter or control transport delay. The control bandwidth was designed to limit transient errors to within 0.1 deg in the presence of a 1.5 inches spacecraft CG offset along the z-axis. The first five out-of-plane modes at nominal frequencies, 0.5% structural damping and 0 deg wing angle were included. Using gyro references, both the first (mode 1) and second out-of-plane mode (mode 3) are phase-stabilized with about 70 deg and 30 deg phase margins, respectively, and the remaining out-of-plane modes (5, 7, 9 & 10) are gain-stabilized with at least 22 dB gain margin. The control design provides a 6.5:1 ratio to the separation between the zero gain crossing frequency and the pole of the first structural mode. Figure 5.2 shows the same design without a structural filter, but with a 2 RTI control transport delay. The transport delay effect can be seen on the structural modes greater than 0.33 Hz, to which the phase lag induced by transport delay was added, yielding almost no phase margin on the second out-of-plane mode. The linear design was then improved with a phase-lead notch filter, which has a unit gain in the low frequency range and a maximum of 68 deg phase lead at the notch frequency of 1.209 Hz. Figure 5.3 shows that the phase margin of the second out-of-plane mode was increased up to 36 deg with the phase-lead notch filter. The notch frequency was carefully selected to ensure that all phase-stabilized modes will remain in the phase stabilization region in the presence of 100% frequency increase as shown in Figure 5.4. Although a 100% frequency increase is allowed before mode 3 loses its phase stabilization characteristics, this mode is also gain stabilized once its frequency increases from the nominal. Also, the third out-of-plane mode (mode 5) is gain stabilized with 13 dB margin at its nominal frequency (1.8627 Hz, system mode). Decreasing the frequency of this mode immediately leads it to the phase stabilization region, while the gain stabilization characteristics are still retained. This mode reaches adequate phase margin before the gain stabilization characteristics vanish at more than 50% frequency drop as shown in Figure 5.5.

The pitch transient during south maneuvers is affected by thrusting disturbance, primarily induced by both the thruster cant angles and the thrust mismatch. The net pitch disturbance is estimated to be 0.4 ft-lb, which requires the 8 msec minimum control pulsewidth to be fired at a rate of 1.667 Hz at which the half sample rate is nearly equal to the first torsional mode. The pitch loop has rigid response in south stationkeeping because the effect of the torsional mode is insignificant about the half sample control rate. The pitch transient during east/west maneuvers is primarily affected by the S/C CG yaw offset from the pressure center of the maneuver thrusters. With a 5.9 inches yaw offset, it requires a 1.5 RTI control pulsewidth to be fired every modulation period. The linear frequency analysis of the spacecraft pitch rate loop in Stationkeeping Mode when the pitch wing dynamics with SWD are in the "constraint" state is shown in Figure 5.6. The design with the same phase-lead notch filter as applied to the roll and yaw loops was based on 2 RTIs control pulsewidth, 2 RTIs control transport delay and 8 RTIs modulation period. The first torsional mode (mode 4) is both phase and gain stabilized at its nominal frequency with 55 deg phase margin and 20 dB gain margin. Either dropping or increasing the frequency produces no impact on stability at all.

Figure 5.7 shows the stability of the first in-plane mode (mode 2) at nominal frequency and with the phase-lead notch filter. It is also phase-stabilized with 46 deg phase margin. This mode remains in the phase stabilization region even with a 100% frequency increase while still having 23° phase margin as shown in Figure 5.8.

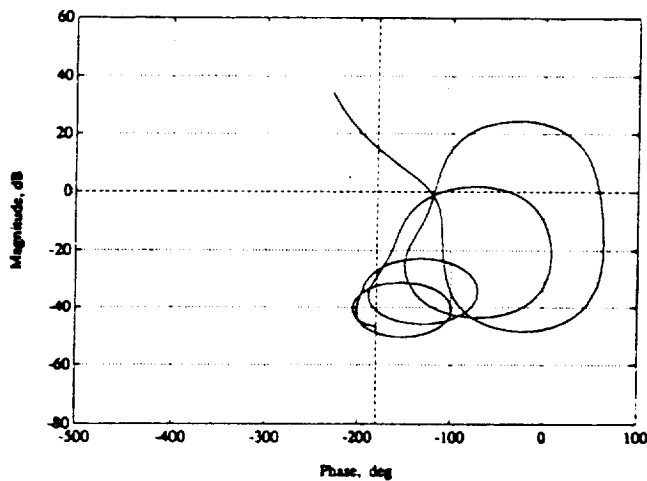
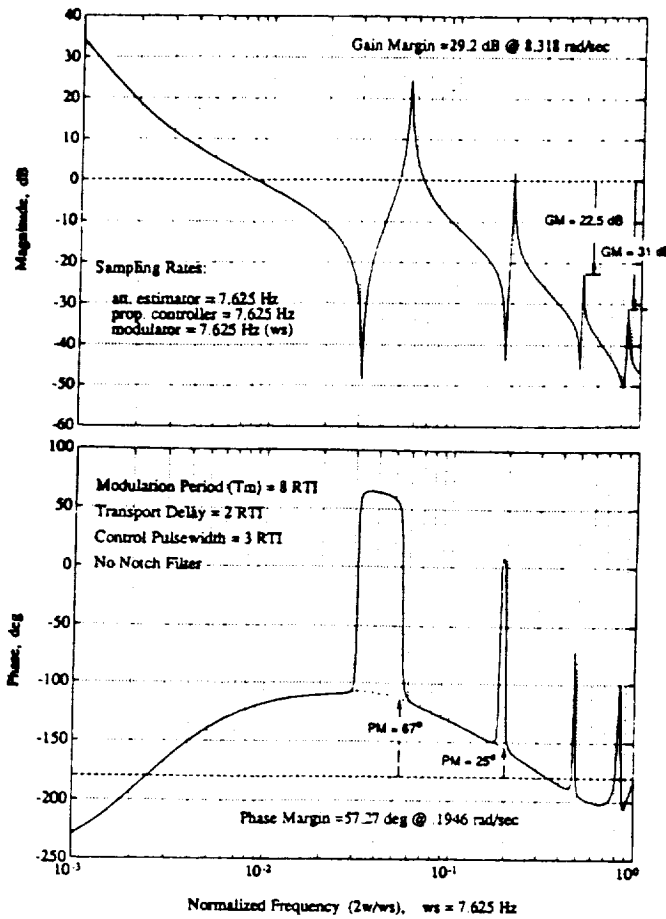


Figure 5.1 Discrete Bode Plots and Nichols Chart of Roll Rate Loop in Stationkeeping Mode at 0.5% Structural Damping, Nominal Frequencies : without Structural Filter and Zero Control Transport Delay

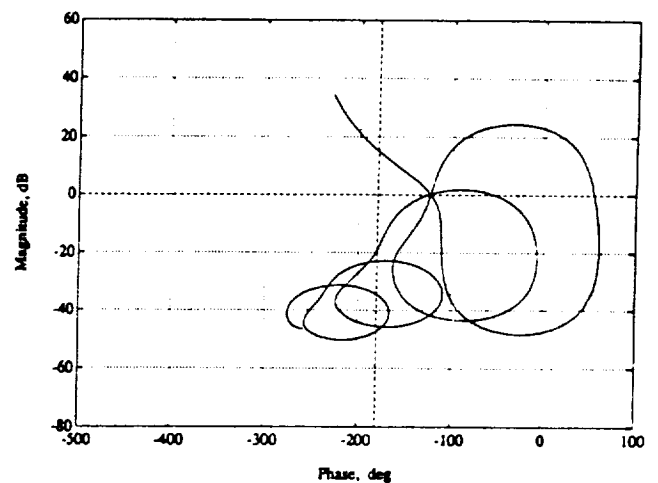
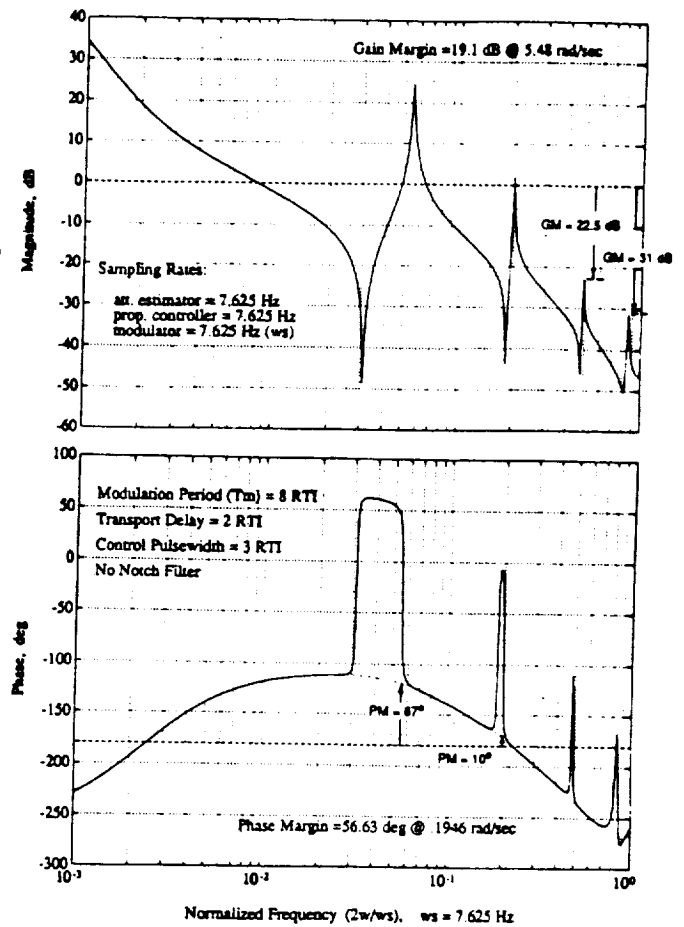


Figure 5.2 Discrete Bode Plots and Nichols Chart of Roll Rate Loop in Stationkeeping Mode at 0.5% Structural Damping, Nominal Frequencies : without Structural Filter, but with 2 RTIs Control Transport Delay

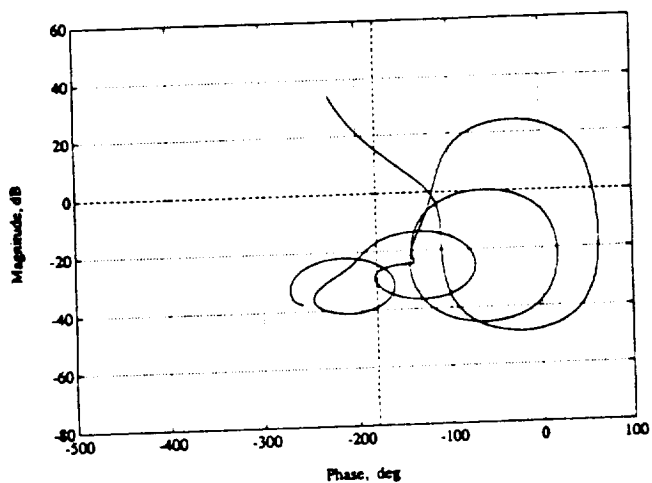
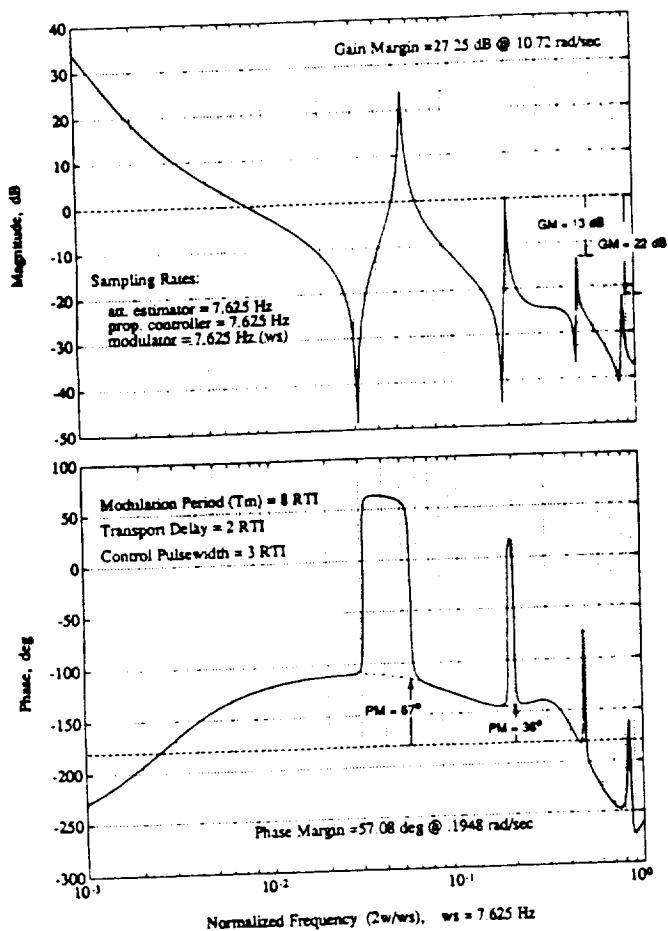


Figure 5.3 Discrete Bode Plots and Nichols Chart of Roll Rate Loop in Stationkeeping Mode at 0.5% Structural Damping, Nominal Frequencies : with Phase-Lead Notch Filter and 2 RTIs Control Transport Delay

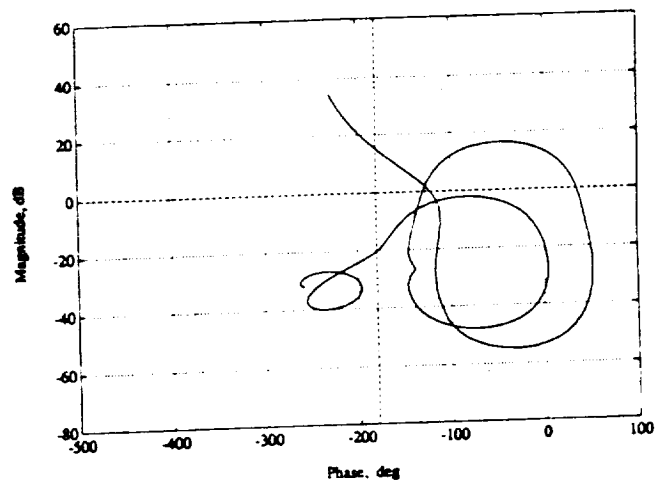
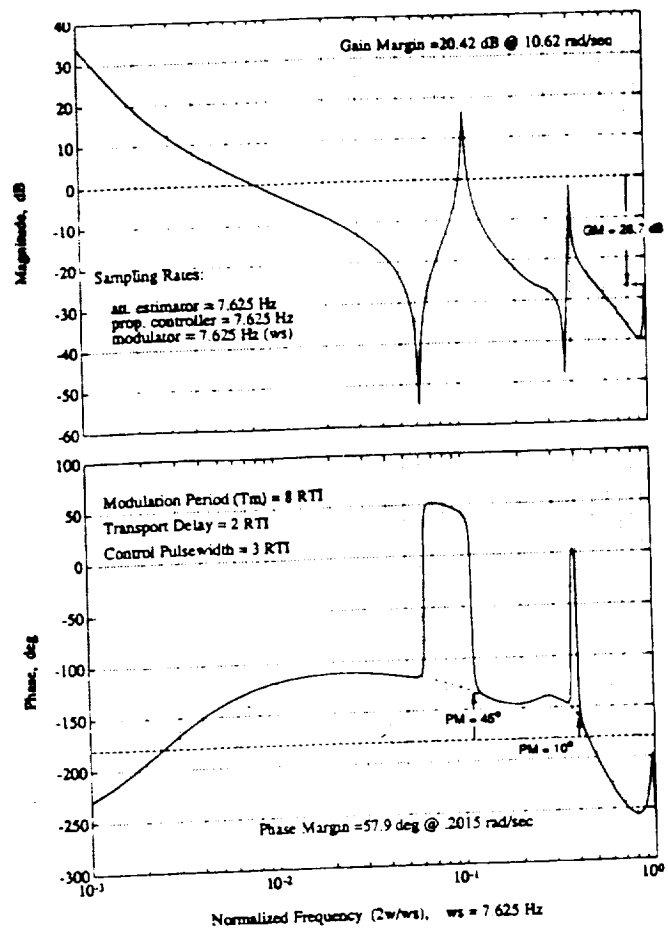


Figure 5.4 Discrete Bode Plots and Nichols Chart of Roll Rate Loop in Stationkeeping Mode at 0.5% Structural Damping, 100% Frequency Increase : with Phase-Lead Notch Filter and 2 RTIs Control Transport Delay

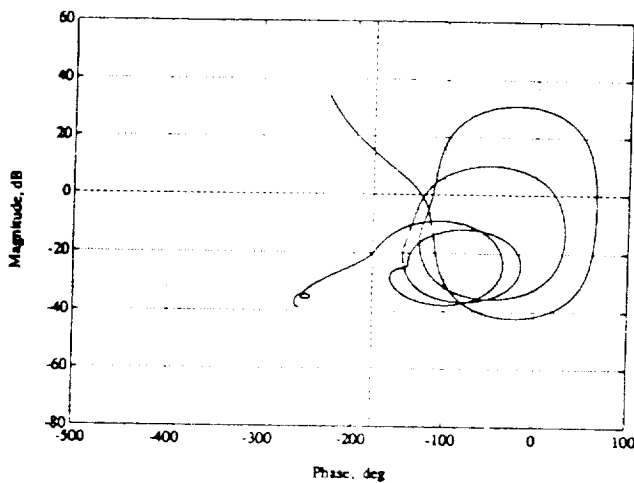
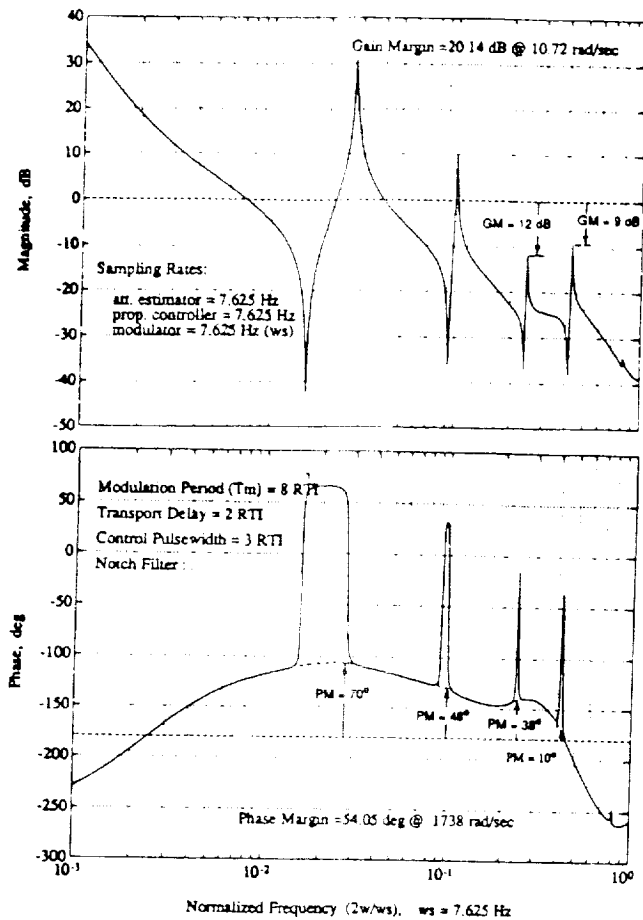


Figure 5.5 Discrete Bode Plots and Nichols Chart of Roll Rate Loop in Stationkeeping Mode at 0.5% Structural Damping, 50% Frequency drop : with Phase-Lead Notch Filter and 2 RTIs Control Transport Delay

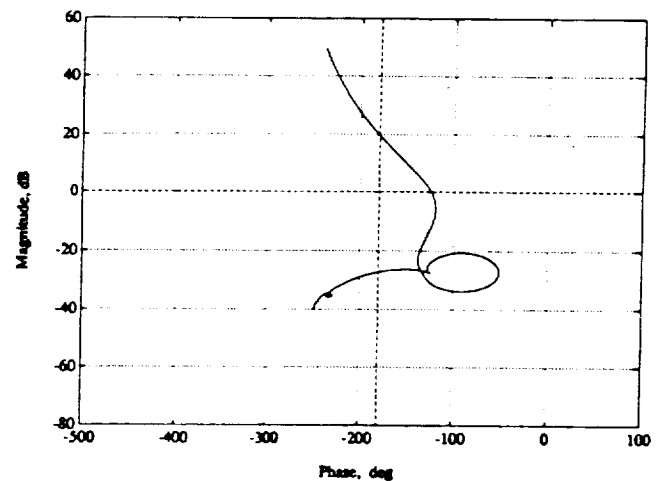
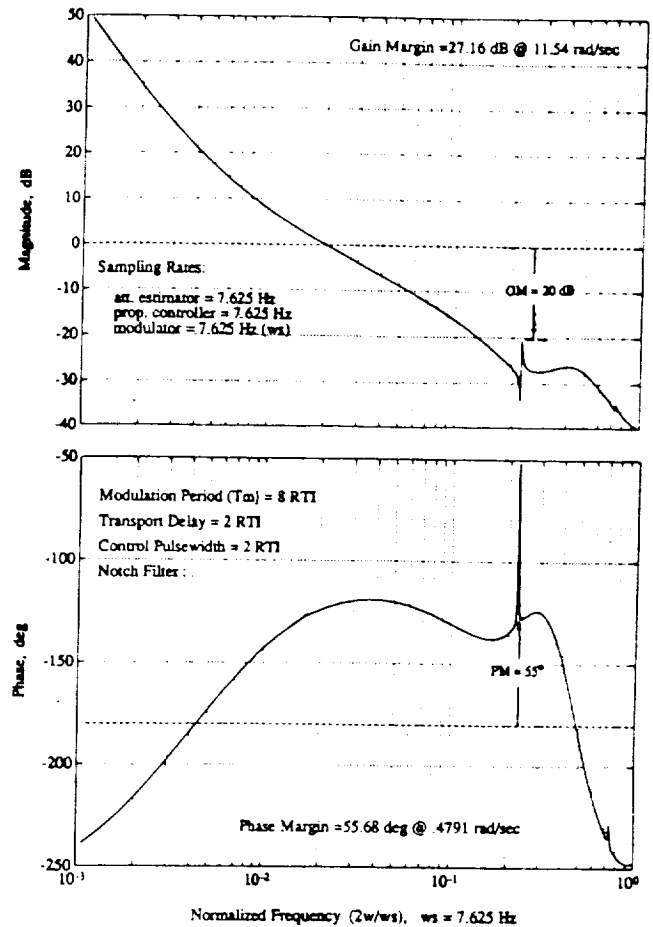


Figure 5.6 Discrete Bode Plots and Nichols Chart of Pitch Rate Loop in Stationkeeping Mode at 0.5% Structural Damping, Nominal Frequencies : with Phase-Lead Notch Filter and 2 RTIs Control Transport Delay

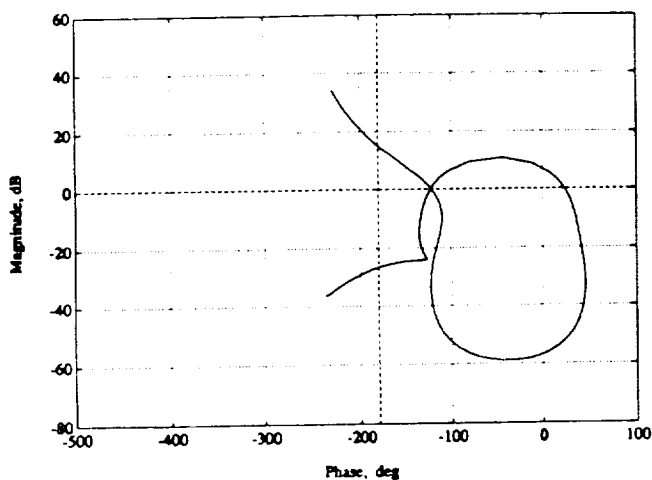
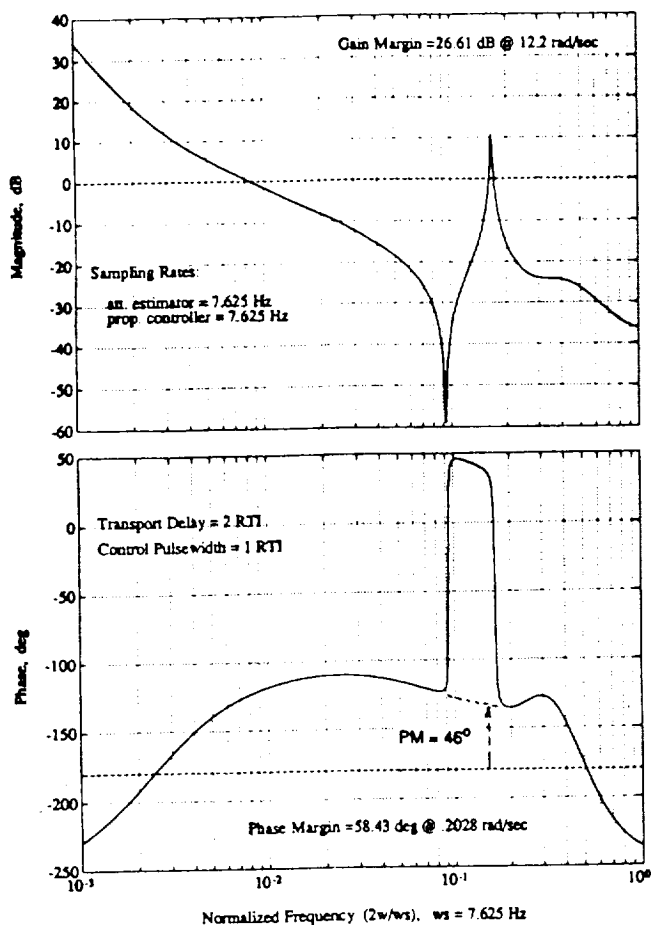


Figure 5.7 Discrete Bode Plots and Nichols Chart of Yaw Rate Loop in Stationkeeping Mode at 0.5% Structural Damping, Nominal Frequencies : with Phase-Lead Notch Filter and 2 RTIs Control Transport Delay

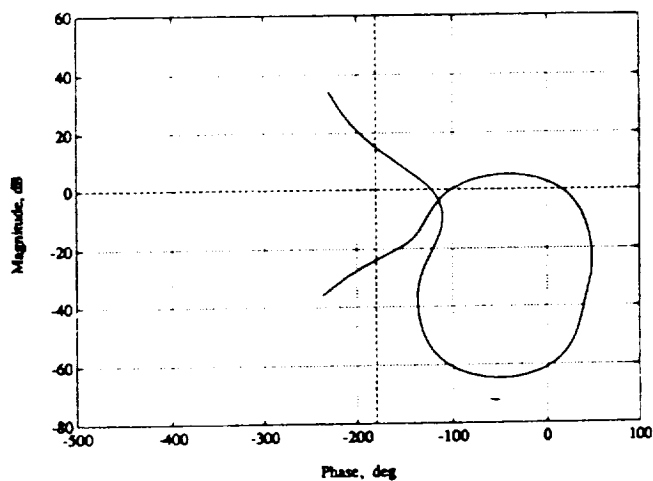
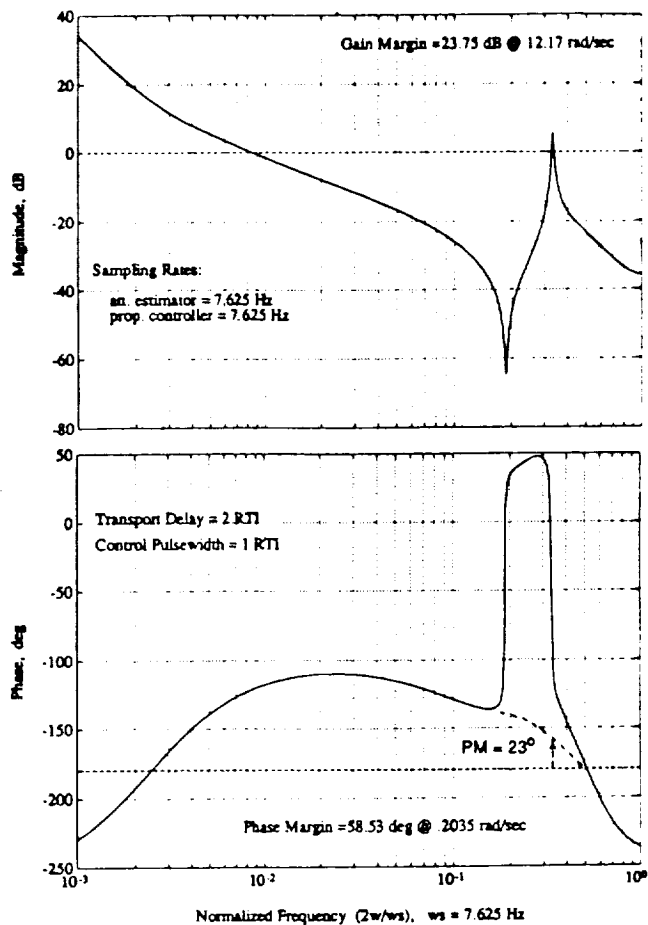


Figure 5.8 Discrete Bode Plots and Nichols Chart of Yaw Rate Loop in Stationkeeping Mode at 0.5% Structural Damping, 100% Frequency Increase : with Phase-Lead Notch Filter and 2 RTIs Control Transport Delay

6. Dynamic Model Validation and Digital Implementation

The main objective is to consider issues dealing with flexibility in multibody dynamics. Multibody dynamics is differentiated from structural dynamics by its capability to undergo arbitrary rigid body motion. Analysis of flexible structures are well established using finite element method within the context of structural dynamics. In multibody dynamics context, need for flexibility modelling arose in recent years as exemplified by large space structures and 3-axes stabilized satellites.

To systematically address the addition of flexible domain, the virtual work principle is chosen as the basis for derivation. The motivation for this choice is based on intended discretization using the finite element method. By choosing the same basis for multibody dynamics and for the finite element method, extensions into nonlinear flexibility is natural and consistent. Other choices are readily available in the literature [1-3].

Virtual Work Principle

An integral representation of the governing equations of motion of solids are imbedded in the virtual work principle. By deriving the multibody dynamics equations via the virtual work principle, a consistent treatment of flexible domain can be made. In practice, the flexible domain is discretized using the finite element method. The virtual work principle is the basis for the finite element method. The technology developed in the finite element method can be integrated into the flexible multibody dynamics efforts.

The virtual work principle states

$$\delta W_{\text{ext}} = \int_V \delta \mathbf{R} \cdot (\mathbf{f} - \rho \ddot{\mathbf{R}}) dV = \delta W_{\text{int}} = \int_V \delta \epsilon : \sigma dV \quad (6.1)$$

where

- \mathbf{R} = material particle position vector wrt inertial frame
- \mathbf{f} = force/unit volume
- ρ = density
- \mathbf{V} = reference configuration
- ϵ = strain
- σ = stress

The main advantages offered by applying the virtual work principle are twofold. First, the integral representation together with the virtual displacements allow domain decomposition between the rigid and the flexible portions of a vehicle. Second, a consistent formulation of a flexible multibody vehicle can be derived and assessed. Consistency refers to final discretization using the finite element method. Once such consistent derivation is made, extensions to nonlinear flexible models can be made by adopting techniques developed in the finite element method [14].

Rigid Body with Attached Flexible Appendage

To further explore the method presented by the virtual work principle, an idealized flexible spacecraft model is derived. The idealization involve representing the spacecraft as a rigid body with attached flexible appendage. The flexible appendage is assumed to be fixed to the rigid body. Articulation is not allowed. Even with this simplifying assumptions, a wide class of vehicles can be modelled.

Consider the idealization shown in Figure 6.1.

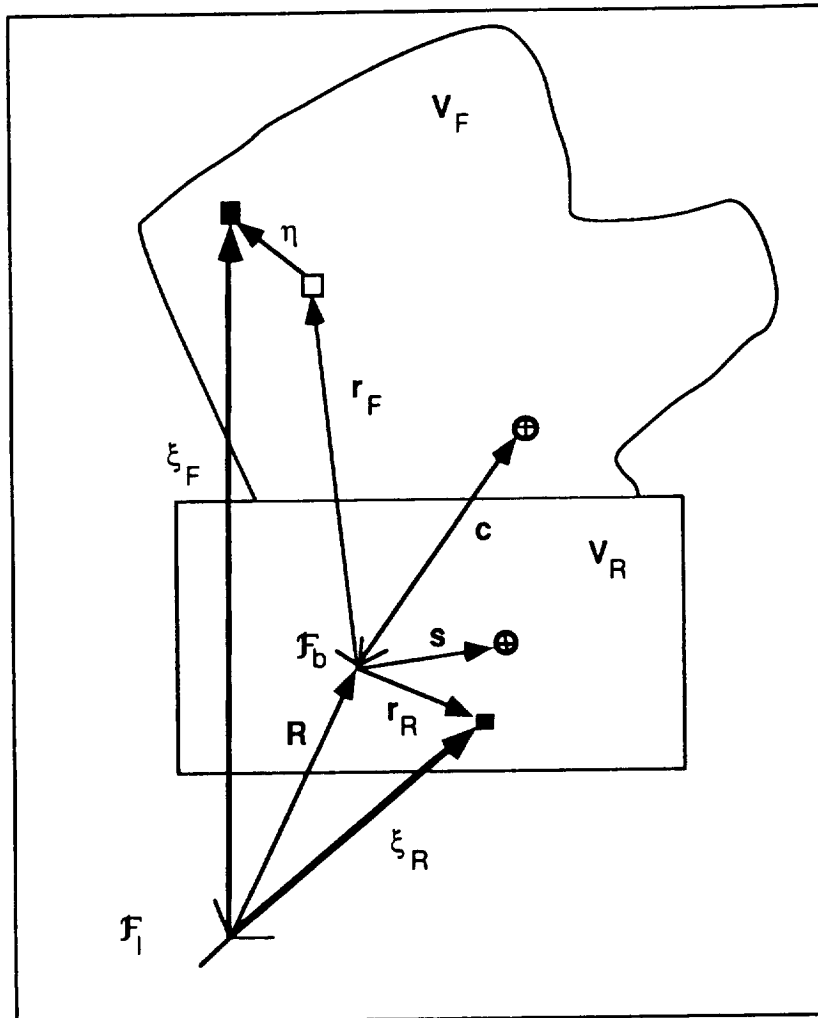


Figure 6.1. Idealized Rigid Body with Flexible Appendage.

The domains, frames, and the position vectors are defined as

- V_F = flexible domain
- V_R = rigid domain
- F_I = inertial frame

- \mathbf{F}_b = body frame
- \mathbf{R} = inertial frame origin to body frame origin
- ξ_R = inertial frame origin to rigid body material particle
- \mathbf{r}_R = body frame origin to rigid body material particle
- \mathbf{s} = body frame origin to rigid body center of mass
- ξ_F = inertial frame origin to flexible material particle
- \mathbf{r}_F = body frame origin to reference material particle position
- η = relative particle displacement
- \mathbf{c} = body frame origin to vehicle center of mass

Application of the virtual work principle to this vehicle yields

$$\int_{V_R} \delta \xi_R \cdot (\mathbf{f} - \rho \ddot{\xi}_R) dV + \int_{V_F} \delta \xi_F \cdot (\mathbf{f} - \rho \ddot{\xi}_F) dV = \int_{V_F} \delta \epsilon : \sigma dV \quad (6.2)$$

with

$$\xi_R = \mathbf{R} + \mathbf{r}_R$$

$$\ddot{\xi}_R = \mathbf{F}_b^T [\ddot{\mathbf{u}} + \underline{\omega} \times \underline{\mathbf{u}} + \dot{\underline{\omega}} \times \underline{\mathbf{r}}_R + \underline{\omega} \times (\underline{\omega} \times \underline{\mathbf{r}}_R)] = \mathbf{F}_b^T \underline{\mathbf{a}}_R$$

$$\delta \xi_R = \mathbf{F}_b^T [\delta \underline{\mathbf{x}} + \delta \underline{\theta} \times \underline{\mathbf{r}}_R]$$

and

$$\xi_F = \mathbf{R} + \mathbf{r}_F + \eta$$

$$\ddot{\xi}_F = \mathbf{F}_b^T [\ddot{\mathbf{u}} + \underline{\omega} \times \underline{\mathbf{u}} + \dot{\underline{\omega}} \times (\underline{\mathbf{r}}_F + \underline{\eta}) + 2 \underline{\omega} \times \underline{\dot{\eta}} + \underline{\omega} \times (\underline{\omega} \times (\underline{\mathbf{r}}_F + \underline{\eta})) + \ddot{\underline{\eta}}] = \mathbf{F}_b^T \underline{\mathbf{a}}_F$$

$$\delta \xi_F = \mathbf{F}_b^T [\delta \underline{\mathbf{x}} + \delta \underline{\theta} \times (\underline{\mathbf{r}}_F + \underline{\eta}) + \delta \underline{\eta}]$$

where

- $\underline{\mathbf{u}}$ = velocity of body frame wrt inertial frame
- $\underline{\omega}$ = angular rate of body frame wrt inertial frame
- $\delta \underline{\mathbf{x}}$ = virtual displacement of the body frame
- $\delta \underline{\theta}$ = virtual rotation of the body frame
- $\delta \underline{\eta}$ = virtual relative displacement

The components, underlined, are defined with respect to the first occurrence of the frame definition. For example, in above definition, the components $\underline{\mathbf{u}}$ and $\underline{\omega}$ are defined in the body frame. For further discussion on this notation is clearly covered in [1]. Note that the virtual quantities are obtained through infinitesimal variation of the current equilibrated state. Substituting the above quantities into Equation (6.1), following three sets of equations, with respect to the body frame, can be derived.

$$\underline{F} = m\dot{\underline{u}} + m\dot{\underline{\omega}} \times \underline{u} + m\dot{\underline{c}} \times \underline{\omega} + m\dot{\underline{\omega}} \times (\underline{\omega} \times \underline{c}) + 2\dot{\underline{\omega}} \times \left(\int_{V_F} \dot{\underline{n}} \rho dV \right) + \left(\int_{V_F} \ddot{\underline{n}} \rho dV \right) \quad (6.3)$$

$$\begin{aligned} \underline{T} = & m\dot{\underline{c}} \times \underline{u} + m\dot{\underline{c}} \times (\underline{\omega} \times \underline{u}) + I\dot{\underline{\omega}} + \underline{\omega} \times I\dot{\underline{\omega}} \\ & + 2 \int_{V_F} (\underline{r}_F + \underline{n}) \times (\underline{\omega} \times \dot{\underline{n}}) \rho dV + \int_{V_F} (\underline{r}_F + \underline{n}) \times \ddot{\underline{n}} \rho dV \end{aligned} \quad (6.4)$$

$$\begin{aligned} \int_{V_F} \delta \underline{n}^T \underline{f}_F dV = & \left(\int_{V_F} \delta \underline{n}^T \rho dV \right) \dot{\underline{u}} + \left(\int_{V_F} \delta \underline{n}^T \rho dV \right) \underline{\omega} \times \underline{u} \\ & + \left(\int_{V_F} \delta \underline{n}^T \dot{\underline{\omega}} \times (\underline{r}_F + \underline{n}) \rho dV \right) + \left(\int_{V_F} \delta \underline{n}^T \underline{\omega} \times (\underline{\omega} \times (\underline{r}_F + \underline{n})) \rho dV \right) \\ & + 2 \left(\int_{V_F} \delta \underline{n}^T (\underline{\omega} \times \dot{\underline{n}}) \rho dV \right) + \left(\int_{V_F} \delta \underline{n}^T \ddot{\underline{n}} \rho dV \right) + \left(\int_{V_F} \delta \underline{\epsilon} : \underline{\sigma} dV \right) \end{aligned} \quad (6.5)$$

with

$$\underline{F} = \underline{F}_b + \int_{V_F} \underline{f}_F dV$$

$$\underline{T} = \underline{T}_b + \int_{V_F} (\underline{r}_F + \underline{n}) \times \underline{f}_F dV$$

where

$$\begin{aligned} \underline{F}_b &= \text{force applied to the rigid body at body frame origin} \\ \underline{T}_b &= \text{torque applied to the rigid body about body frame origin} \\ I &= \text{instantaneous vehicle inertia matrix wrt body frame origin} \end{aligned}$$

Often in practice, the integral representation in Equations (6.3) - (6.5) is skipped by assuming the lumped mass idealization. However, the discretization of the flexible domain into finite element idealization stem from these equations. The lumped mass idealization is an extreme case. Such inconsistent assumption with finite element method may produce inaccurate results for crude finite element mesh. More systematic study should be made to assess the consequence of such assumption.

As closure, the lumped mass idealization will be made to produce a set of equations that may be compared to previous derivation [4]. The lumped mass idealization takes the volume integral and cast it into a sum spanning the total number of nodes in a finite element mesh. For an arbitrary function, this idealization can be expressed as

$$\int_{V_F} f(\mathbf{n}, \dot{\mathbf{n}}, \ddot{\mathbf{n}}) \rho \, dV = \sum_i f(\mathbf{q}_i, \dot{\mathbf{q}}_i, \ddot{\mathbf{q}}_i) m_i$$

where

\mathbf{q}_i = finite element nodal displacement vector
 m_i = corresponding lumped mass

Adopting this idealization, Equations (6.3) - (6.5) can be reduced to

$$\mathbf{F} = m\dot{\mathbf{u}} + m\boldsymbol{\omega} \times \mathbf{u} + m\dot{\boldsymbol{\omega}} \times \mathbf{c} + m\boldsymbol{\omega} \times (\boldsymbol{\omega} \times \mathbf{c}) + 2 \sum_i m_i \boldsymbol{\omega} \times \dot{\mathbf{q}}_i + \sum_i m_i \ddot{\mathbf{q}}_i \quad (6.6)$$

$$\begin{aligned} \mathbf{T} = & m\mathbf{c} \times \dot{\mathbf{u}} + m\mathbf{c} \times (\boldsymbol{\omega} \times \mathbf{u}) + I\dot{\boldsymbol{\omega}} + \boldsymbol{\omega} \times I\boldsymbol{\omega} \\ & + 2 \sum_i m_i (\mathbf{r}_i + \mathbf{q}_i) \times (\boldsymbol{\omega} \times \dot{\mathbf{q}}_i) + \sum_i m_i (\mathbf{r}_i + \mathbf{q}_i) \times \ddot{\mathbf{q}}_i \end{aligned} \quad (6.7)$$

$$\begin{aligned} \mathbf{f}_i = & m_i \dot{\mathbf{u}} + m_i \boldsymbol{\omega} \times \mathbf{u} + m_i \dot{\boldsymbol{\omega}} \times (\mathbf{r}_i + \mathbf{q}_i) + m_i \boldsymbol{\omega} \times (\boldsymbol{\omega} \times (\mathbf{r}_i + \mathbf{q}_i)) \\ & + 2 m_i \boldsymbol{\omega} \times \dot{\mathbf{q}}_i + m_i \ddot{\mathbf{q}}_i + \sum_j K_{ij} \mathbf{q}_j \end{aligned} \quad (6.8)$$

where

m = total vehicle mass
 K_{ij} = assembled stiffness matrix

By interpreting the stiffness matrix as the tangent stiffness matrix, the equations are valid for nonlinear flexible systems. Since modal reduction generally is not possible for nonlinear flexible systems, the finite element nodal degrees of freedom must be used to represent flexible degrees of freedom. For linear flexible system, an indepth coverage of an alternate derivation of Equations (6.6) - (6.8) is provided in [4].

Extending Symbolic Rigid Body Code to include Flexibility

In the recent years symbolic manipulation software capable of generating rigid body code became available. Some example of such codes are SD/FAST (Symbolic Dynamics, Inc.) [6], AUTOLEV (OnLine Dynamics, Inc.) [8], and AUTOSIM (Univ. of Michigan) [9]. For rigid vehicles, these tools can dramatically reduce the time spent on deriving and implementing the equations of motion.

By combining the codes generated by the symbolic manipulation software with reduced set of "hand" derived equations addressing the flexible domain, the capability of these codes can be extended to flexible vehicles. A systematic method for such an extension is provided for a satellite class of flexible vehicles. This method will be

illustrated with previously derived equations of motion for a rigid body with flexible appendages.

For a rigid body with flexible appendages, the resulting equations can be partitioned into

$$\begin{bmatrix} A & B \\ B^T & 1 \end{bmatrix} \begin{Bmatrix} \ddot{u}_R \\ \ddot{u}_F \end{Bmatrix} = \begin{Bmatrix} R_R + R_{RF} \\ R_F \end{Bmatrix} \quad (6.9)$$

where

$$\begin{aligned} u_R &= \text{rigid degrees of freedom} \\ u_F &= \text{modal amplitude degrees of freedom} \end{aligned}$$

and

$$B = [P \ Q]$$

Note that the P and Q submatrices are defined in the previous section. In Equation (6.9), a modal reduction has been assumed. The portion of the partitioned equation generated by a symbolic manipulation software is

$$[A] \{\ddot{u}_R\} = \{R_R\} \quad (6.10)$$

This portion is obtained by supplying the symbolic manipulation software information on the current configuration. In another words, the total vehicle is assumed to be rigid. The requirement of current configuration entails configuration update at each integration step. The current configuration is the reference configuration.

The solution process follows by forming

$$\{\ddot{u}_F\} = \{R_F\} - [B^T] \{\ddot{u}_R\} \quad (6.11)$$

and substituting into the rigid partition to yield

$$[A - BB^T] \{\ddot{u}_R\} = \{R_R + R_{RF}\} - [B] \{R_F\} \quad (6.12)$$

In terms of actual equations of motion, by observing the structure of Equations (6.4) - (6.6), the necessary additional partitions can be generated by discretization and modal reduction of the terms

$$\begin{pmatrix} \left(\int_{v_F} \ddot{\eta} \rho dV \right) \\ \left(\int_{v_F} (\mathbf{r}_F + \boldsymbol{\eta}) \times \ddot{\eta} \rho dV \right) \end{pmatrix} \rightarrow [\mathbf{B}] \{\ddot{u}_F\} \quad (6.13)$$

$$\begin{pmatrix} \left(\int_{v_F} \mathbf{f}_F dV \right) \\ \left(\int_{v_F} (\mathbf{r}_F + \boldsymbol{\eta}) \times \mathbf{f}_F dV \right) \end{pmatrix} - \begin{pmatrix} 2 \boldsymbol{\omega} \times \left(\int_{v_F} \dot{\eta} \rho dV \right) \\ \left(2 \int_{v_F} (\mathbf{r}_F + \boldsymbol{\eta}) \times (\boldsymbol{\omega} \times \dot{\eta}) \rho dV \right) \end{pmatrix} \rightarrow \{\mathbf{R}_{RF}\} \quad (6.14)$$

The flexible partition can be generated by Equation (6.5).

Methodology presented above produces an "exact" set of equations. Standard assumptions such as constant vehicle center of mass and inertia together with small relative flexible displacements can be made as deemed plausible to reduce computational effort.

Rigid Body with Articulated Flexible Appendages

With assumption that an symbolic manipulation software will be used to generate the rigid partition of the equation of motion, only the required matrices for the articulated flexible domain will be documented. The idealized articulated flexible appendage is shown in Figure 6.2.

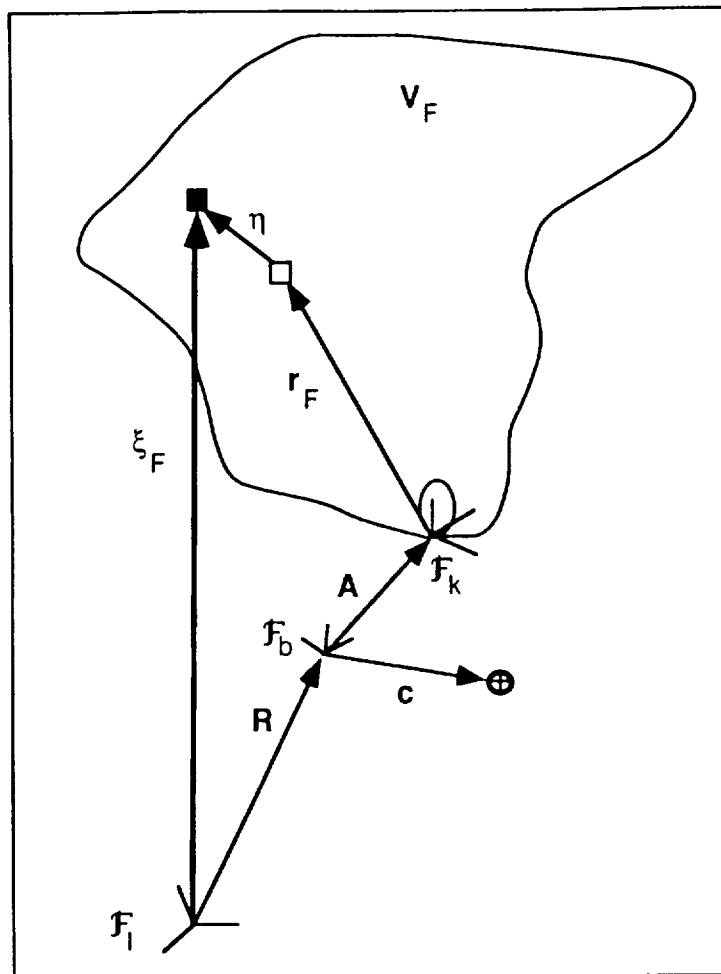


Figure 6.2. Idealized Articulated Flexible Appendage.

The quantities are defined as

- V_F = flexible domain
- \mathcal{F}_I = inertial frame
- \mathcal{F}_b = body frame
- \mathcal{F}_k = appendage frame imbedded in the yoke body
- \mathbf{R} = inertial frame origin to body frame origin
- \mathbf{A} = body frame origin to appendage frame origin
- ξ_F = inertial frame origin to flexible material particle
- \mathbf{r}_F = appendage frame origin to reference material particle position
- $\boldsymbol{\eta}$ = relative particle displacement
- \mathbf{c} = body frame origin to vehicle center of mass

In generating the rigid partition using a symbolic manipulation software, consider the yoke body and the flexible domain as a single rigid body defined in the current configuration.

Application of the virtual work principle to the flexible appendage yields

$$\int_{v_F} \delta \xi_F \cdot (\mathbf{f} - \rho \ddot{\xi}_F) dV = \int_{v_F} \delta \epsilon : \sigma dV \quad (6.15)$$

with

$$\xi_F = \mathbf{R} + \mathbf{A} + \mathbf{r}_F + \boldsymbol{\eta} \equiv \mathbf{F}_I^T \mathbf{R} + \mathbf{F}_b^T \mathbf{A} + \mathbf{F}_k^T (\mathbf{r}_F + \boldsymbol{\eta})$$

$$\begin{aligned} \ddot{\xi}_F &= \mathbf{F}_b^T [\dot{\mathbf{u}} + \boldsymbol{\omega}_b \times \mathbf{u} + \dot{\boldsymbol{\omega}}_b \times \mathbf{A} + \boldsymbol{\omega}_b \times (\boldsymbol{\omega}_b \times \mathbf{A})] \\ &+ \mathbf{F}_k^T [\dot{\boldsymbol{\omega}}_k \times (\mathbf{r}_F + \boldsymbol{\eta}) + 2 \boldsymbol{\omega}_k \times \dot{\boldsymbol{\eta}} + \boldsymbol{\omega}_k \times (\boldsymbol{\omega}_k \times (\mathbf{r}_F + \boldsymbol{\eta})) + \ddot{\boldsymbol{\eta}}] \equiv \mathbf{F}_b^T \mathbf{a}_b \equiv \mathbf{F}_k^T \mathbf{a}_k \end{aligned}$$

$$\delta \xi_F = \mathbf{F}_b^T [\delta \mathbf{x} + \delta \boldsymbol{\theta}_b \times \mathbf{A}] + \mathbf{F}_k^T [\delta \boldsymbol{\theta}_k \times (\mathbf{r}_F + \boldsymbol{\eta}) + \delta \boldsymbol{\eta}]$$

where

- \mathbf{u} = velocity of body frame wrt inertial frame
- $\boldsymbol{\omega}_b$ = angular rate of body frame wrt inertial frame
- $\boldsymbol{\omega}_k$ = angular rate of appendage frame wrt inertial frame
- $\delta \mathbf{x}$ = virtual displacement of the body frame
- $\delta \boldsymbol{\theta}_b$ = virtual rotation of the body frame
- $\delta \boldsymbol{\theta}_k$ = virtual rotation of the appendage frame
- $\delta \boldsymbol{\eta}$ = virtual relative displacement

The appendage angular rate can be decomposed into

$$\boldsymbol{\omega}_k = \mathbf{F}_k^T \boldsymbol{\omega}_k = \boldsymbol{\omega}_b + \boldsymbol{\omega}_{bk} = \mathbf{F}_b^T \boldsymbol{\omega}_b + \mathbf{F}_k^T \boldsymbol{\omega}_{bk} \quad (6.16)$$

Similarly,

$$\delta \boldsymbol{\theta}_k = \mathbf{F}_k^T \delta \boldsymbol{\theta}_k = \mathbf{F}_b^T \delta \boldsymbol{\theta}_b + \mathbf{F}_k^T \delta \boldsymbol{\theta}_{bk} \quad (6.17)$$

where

- $\boldsymbol{\omega}_{bk}$ = relative angular rate of appendage frame wrt body frame
- $\delta \boldsymbol{\theta}_{bk}$ = relative virtual rotation of the appendage frame wrt body frame

The frames are transformed with

$$\mathbf{f}_b = \mathbf{C}_{bk} \mathbf{f}_k \quad (6.18)$$

Corresponding to Equation (6.9), the rigid degrees of freedom define

$$\{\ddot{\mathbf{u}}_R\} = \begin{Bmatrix} \ddot{\mathbf{u}} \\ \dot{\boldsymbol{\omega}}_b \\ \dot{\boldsymbol{\omega}}_{bk} \end{Bmatrix} \quad (6.19)$$

Substitution into Equation (6.15) yields following relations.

$$\begin{Bmatrix} \left(\int_{V_F} \mathbf{C}_{bk} \ddot{\mathbf{n}} \rho dV \right) \\ \left(\int_{V_F} [\mathbf{A} \times (\mathbf{C}_{bk} \ddot{\mathbf{n}}) + \mathbf{C}_{bk} ((\mathbf{r}_F + \mathbf{n}) \times \ddot{\mathbf{n}})] \rho dV \right) \\ \left(\int_{V_F} ((\mathbf{r}_F + \mathbf{n}) \times \ddot{\mathbf{n}} \rho dV \right) \end{Bmatrix} \rightarrow [\mathbf{B}] \{\ddot{\mathbf{u}}_F\} \quad (6.20)$$

$$\begin{Bmatrix} \left(\int_{V_F} \mathbf{C}_{bk} \mathbf{f}_F dV \right) \\ \left(\int_{V_F} (\mathbf{A} + \mathbf{C}_{bk} (\mathbf{r}_F + \mathbf{n})) \times (\mathbf{C}_{bk} \mathbf{f}_F) dV \right) \\ \left(\int_{V_F} ((\mathbf{r}_F + \mathbf{n}) \times \mathbf{f}_F dV \right) \end{Bmatrix}$$

$$\begin{Bmatrix} \left(2 \int_{V_F} \mathbf{C}_{bk} (\boldsymbol{\omega}_k \times \dot{\mathbf{n}}) \rho dV \right) \\ \left(2 \int_{V_F} \mathbf{A} \times (\mathbf{C}_{bk} (\boldsymbol{\omega}_k \times \dot{\mathbf{n}})) + \mathbf{C}_{bk} ((\mathbf{r}_F + \mathbf{n}) \times (\boldsymbol{\omega}_k \times \dot{\mathbf{n}})) \rho dV \right) \\ \left(2 \int_{V_F} ((\mathbf{r}_F + \mathbf{n}) \times (\boldsymbol{\omega}_k \times \dot{\mathbf{n}})) \rho dV \right) \end{Bmatrix} \rightarrow \{\mathbf{R}_{RF}\} \quad (6.21)$$

The equations for the flexible domain results in

$$\int_{V_F} \delta \underline{\eta}^T \underline{f}_F dV = \int_{V_F} \delta \underline{\eta}^T \underline{a}_k \rho dV + \int_{V_F} \delta \underline{\epsilon} : \underline{\sigma} dV \quad (6.22)$$

Equations (6.20) - (6.22) yield necessary equations to generate the full equations of motion for a vehicle with articulated flexible appendage. All terms are retained. Vehicle specific truncation of nonlinear terms should be made to these equations. Detailed derivation using an alternate approach of a vehicle with articulated flexible appendage is provided in [5].

Validation

To validate the concept of mating flexible domain equations with code generated using a symbolic manipulation software, the HS-601 satellite [5] is chosen for implementation. AUTOLEV software generated the rigid body portion of the code. Rest of the code that deals with flexible domain has to be coded by the user.

The specific example applies 40 ft-lbs of torque about the roll-axis for .1 sec. The magnitude of the torque characterizes the authority of the reaction control thrusters. The angular positions and rates are shown in Figures 6.3 - 6.4. The results are identical to the previous simulation that was implemented using the derivation described in [5]. Note that the response shown characterizes an actual vehicle. The effects of the flexibility are pronounced. In the rate plots, the magnitude of the rates peak at about 4 times the rate expected for a rigid vehicle with same applied torque.

The use of a symbolic manipulation software with flexible domain equations offers large time saving in terms of both derivation and implementation. In this context, this approach is practical as an engineering tool.

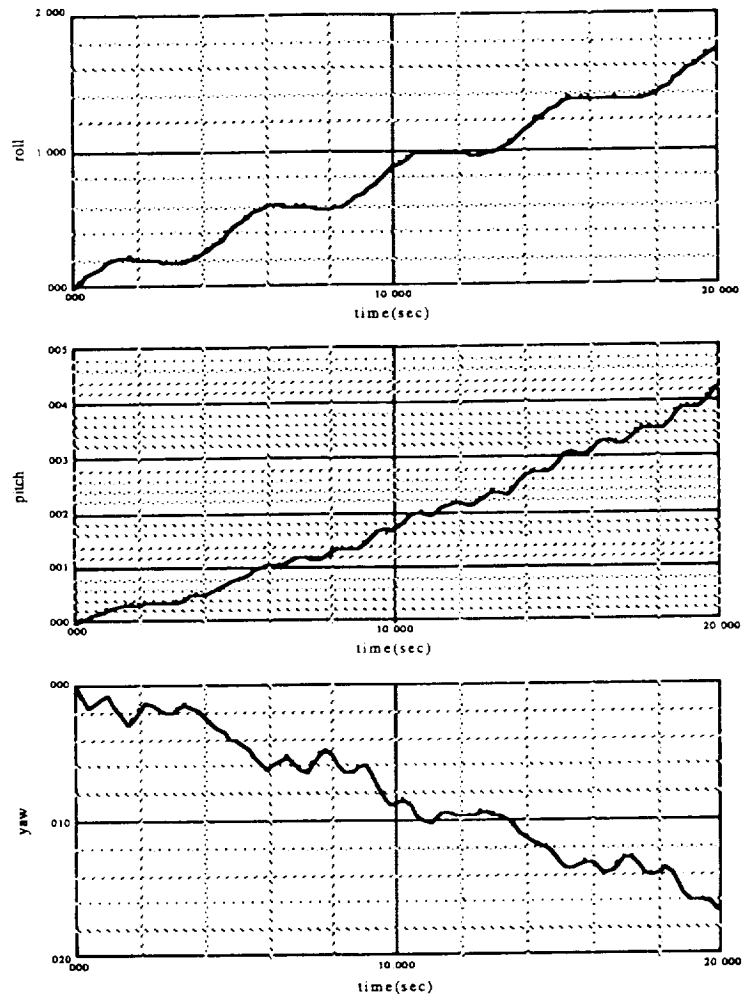


Figure 6.3. Angular Position (deg).

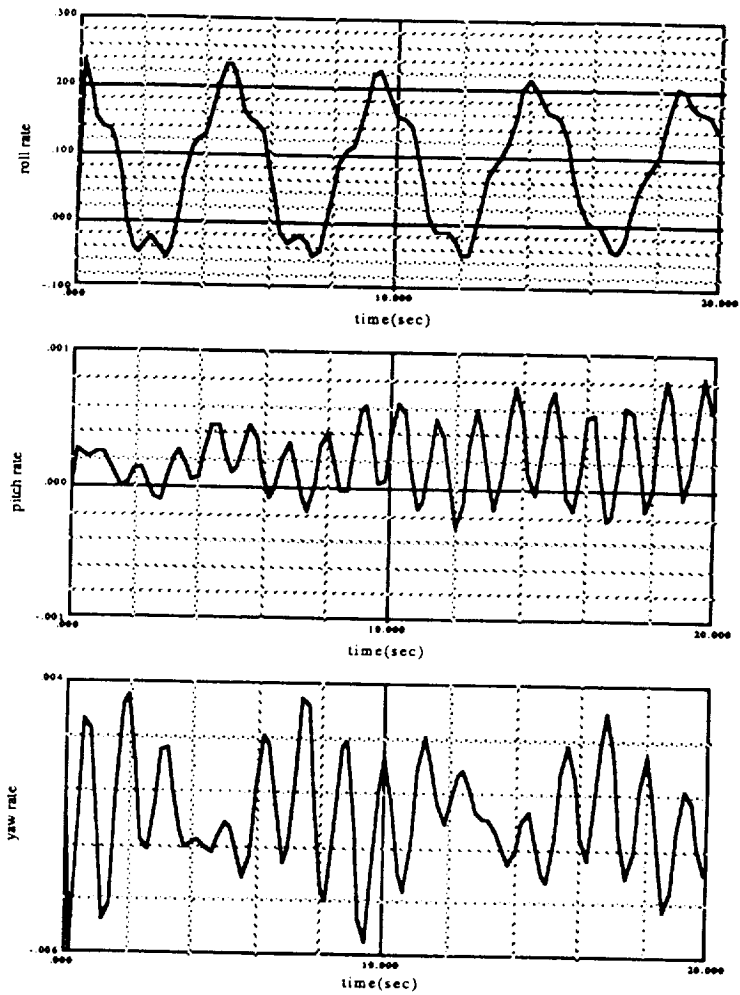


Figure 6.4. Angular Rate (deg/sec).

7. Simulation Performance

Digital simulations employing the hybrid dynamic model with the complete, nonlinear body-stabilized dynamics have been performed to demonstrate the stationkeeping control performance. Key simulation parameters which were added to produce worst case transient errors are: (1) 1.0 inches spacecraft CG offset from the pressure center of the south maneuver thrusters along the z-axis, (2) 5 lbf thrusters with 5% thrust mismatch producing the worst case acceleration disturbance, (3) 1.0 deg thruster misalignment in the direction adding disturbance, (4) flexible north and south wings at 0 deg wing angle, (5) 2 RTI control transport delay, (6) solar wing drive with ± 0.25 deg deadband, (7) thruster EPW (Electrical Impulse Width) error model, which computes the thruster impulse on time delay as a function of time since last pulse. To accommodate the control loss due to EPW error, a fixed 4 msec thruster delay compensation was added to the command pulsewidth, (8) 8 msec pulsing constraint, (9) momentum wheel spinning at 45 ft-lb-sec throughout maneuver, (10) 0.035 deg sample to sample three sigma earth sensor noise, and (11) gyro sensor noises: rate random walk at $\text{PSD} = (10^{-7} \text{ d/s}^2)^2/\text{Hz}$, angle random walk at $\text{PSD} = (10^{-4} \text{ d/s}^2)^2/\text{Hz}$, angle noise at $\text{PSD} = (1.3 \times 10^{-5} \text{ d/s}^2)^2/\text{Hz}$ and quantization of 0.3 arcsec.

With nominal structural mode frequencies and 0.5% structural damping, Figure 7.1 shows the Stationkeeping Mode control performance from a 100-sec south maneuver. The spacecraft angular position and rate along with their estimates about each control axis are plotted. It also shows the acceleration bias estimate and the control acceleration command about each axis. The acceleration bias estimates in this run were initialized to zero. The roll transient, which was induced primarily by the spacecraft yaw CG offset and the thrust mismatch, reaches 0.09 deg, while the yaw transient was primarily due to the thrust mismatch and was about 0.045 deg. The pitch transient induced by the combined effect of canted and thrust mismatch is 0.01 deg. In the steady state, a limit cycle about the pitch axis resulted from the 8 msec thrusting constraint. The acceleration bias estimation converges within 5 sec, showing a smooth bias estimate in the steady state. Transient errors can be improved with an initialization of the acceleration bias estimates to their steady state values. Figure 7.2 shows the performance with both the roll and yaw acceleration bias estimates initialized to 4.5% off their steady state values. Due to an over estimate of the thrusting bias by 4.5%, the roll and yaw attitude were over controlled, yielding transients up to 0.06 deg and 0.042 deg, respectively, in the direction opposite to Figure 7.1. Ideally, a perfect initialization would result in a significant reduction to the roll and yaw transients.

Effects of structural mode uncertainty and damping were also investigated through simulations. Figure 7.3 shows the performance with a 100% frequency increase to each mode, and Figure 7.4 a 50% frequency drop. In both cases, a 0.25% structural damping was assumed. A 50% (Δ) frequency error is equivalent to a 75% $[= 1 - (1 - \Delta)^2]$ change to stiffness of the flexible wings. It is not expected that the structural modes at the on orbit deployed condition would exceed more than 20% from the nominals. Likewise, the structural damping nominally exceeds 0.5%. The modal errors given above are to demonstrate the robustness of the control system. The simulation results show that variations in modal parameters have no major effects on the modal stability nor degrade the pointing performance.

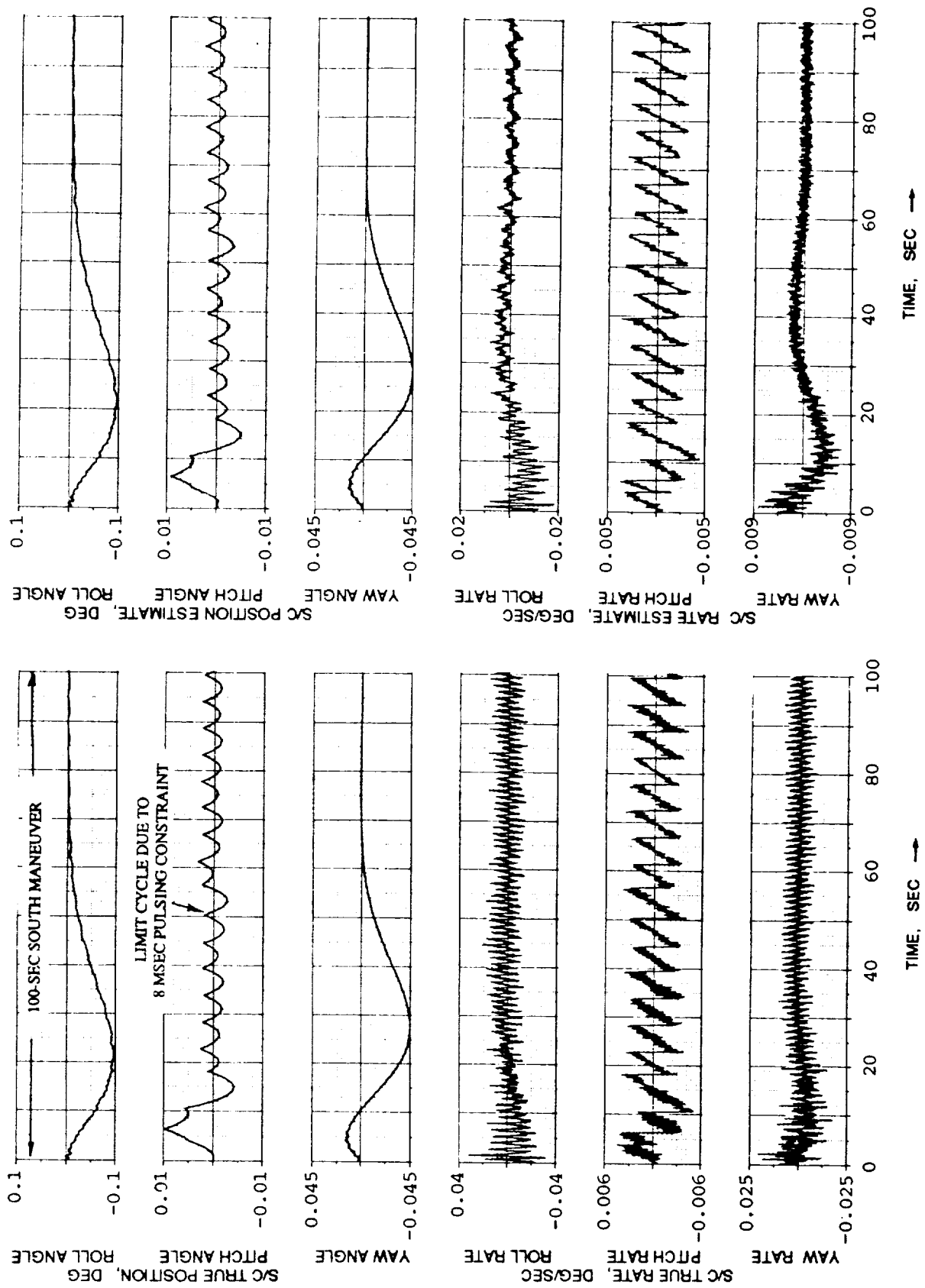


Figure 7.1 Stationkeeping Mode Control Performance From A 100-sec South Maneuver with Zero Initial Acceleration Bias Estimates - Nominal Modal Frequencies, 0.5% Structural Damping

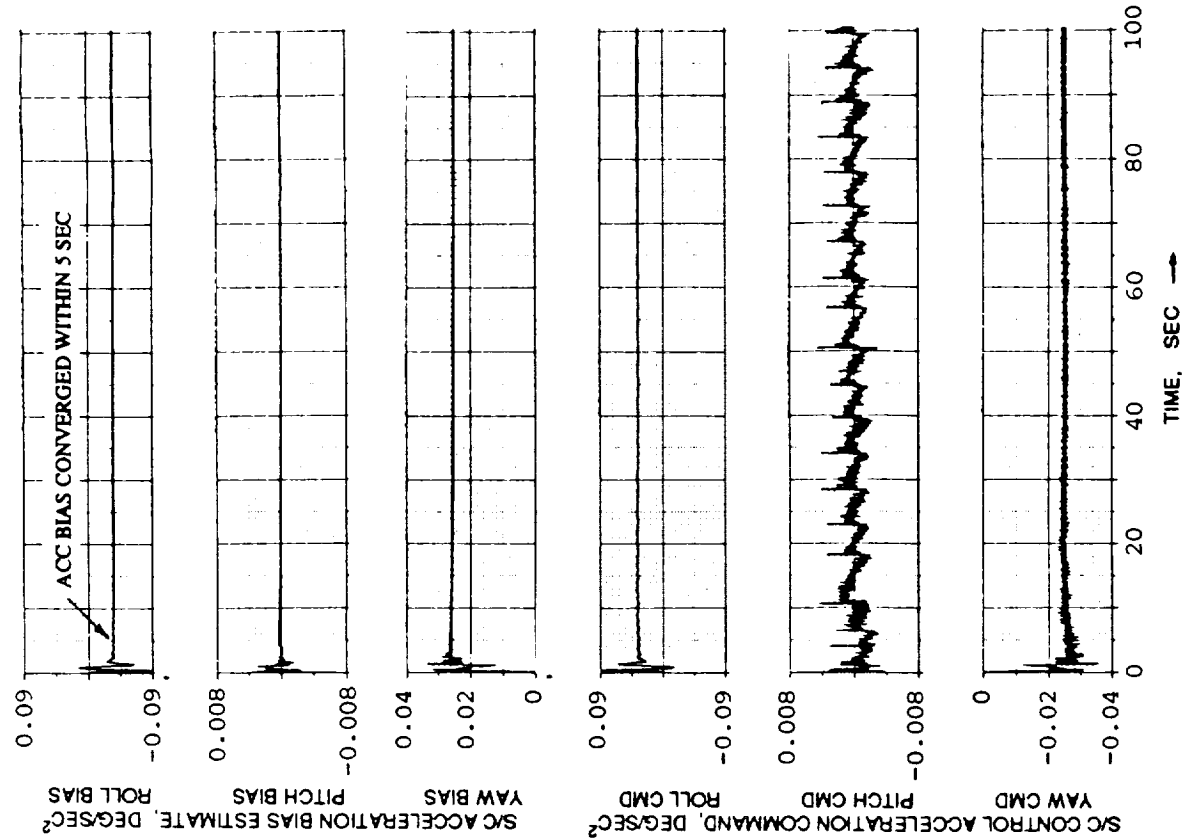


Figure 7.1 (continued)

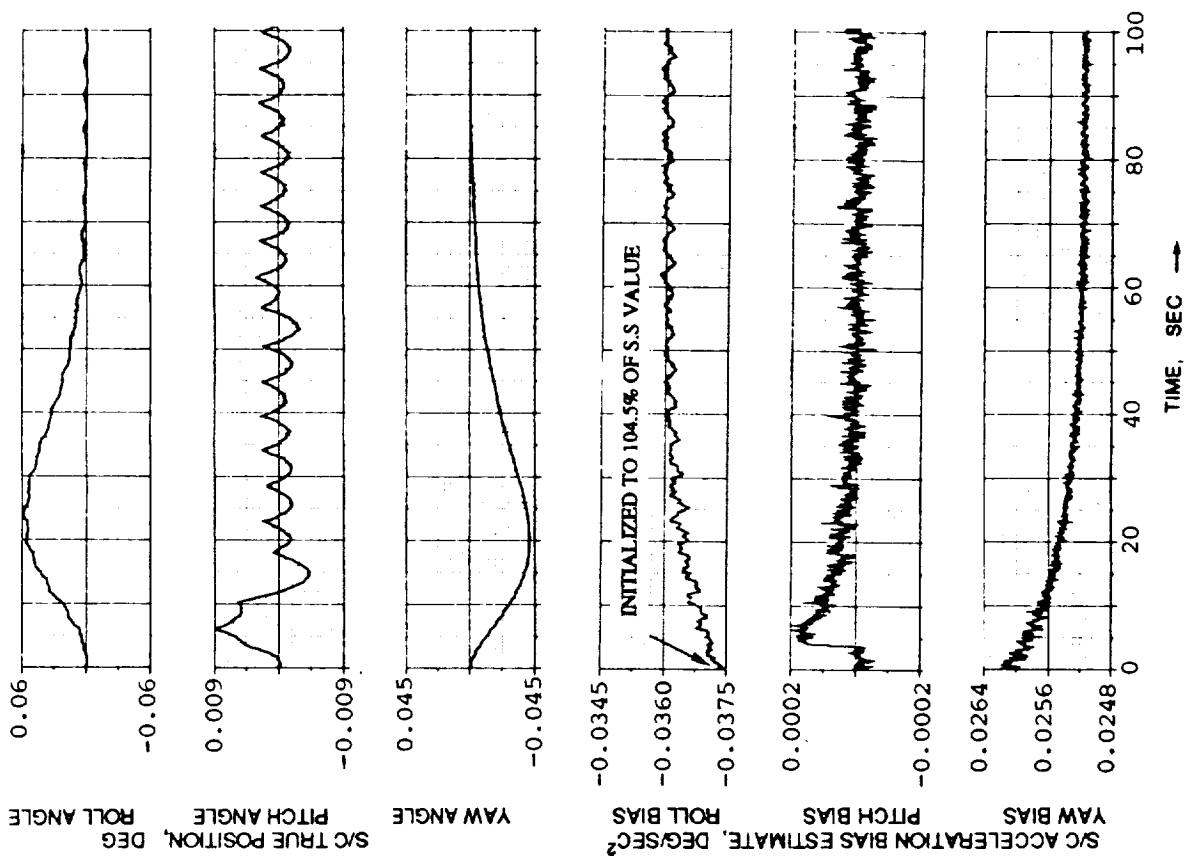


Figure 7.2 Stationkeeping Mode Control Performance From A 100 -sec South Maneuver with Acceleration Bias Estimates Initialized to 4.5% off Steady State Values - Nominal Modal Frequencies, 0.5% Structural Damping

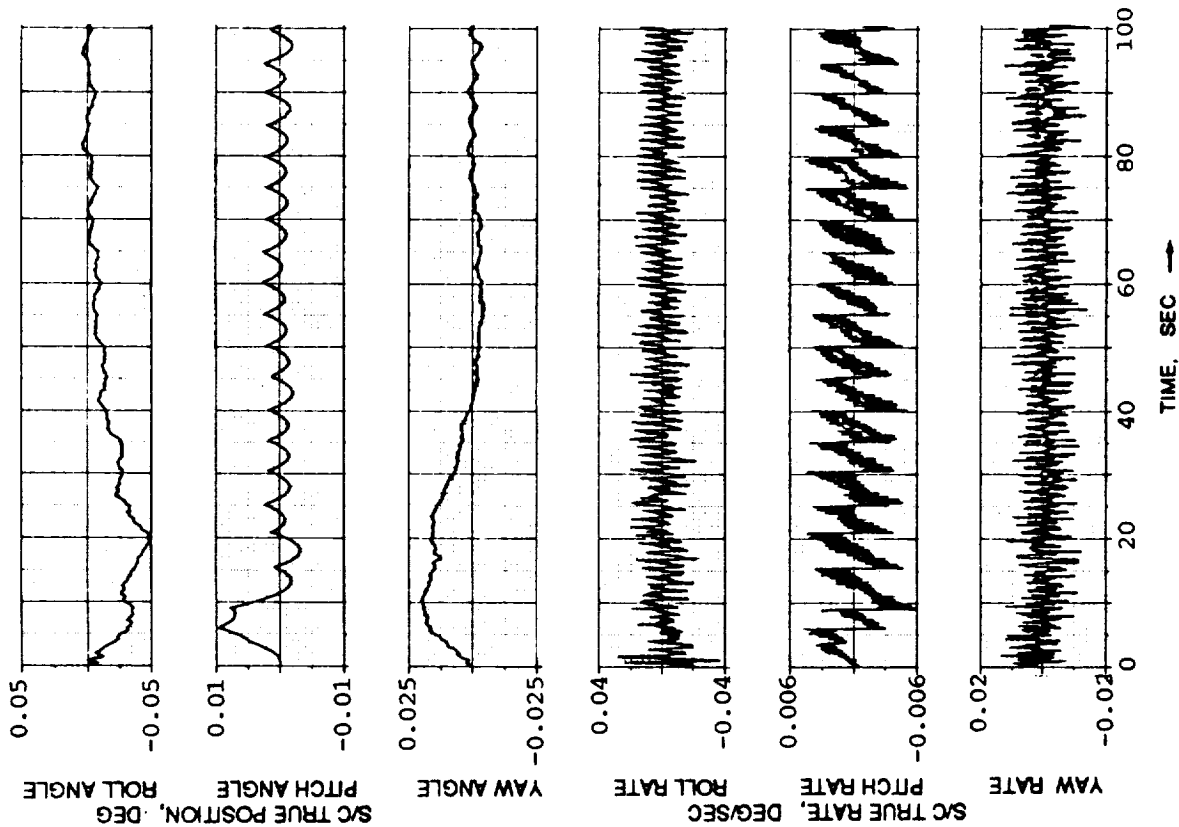


Figure 7.4 Stationkeeping Mode Control Performance From A 100 -sec South Maneuver with Zero Initial Acceleration Bias Estimates - 50% Modal Frequency drop, 0.25% Structural Damping

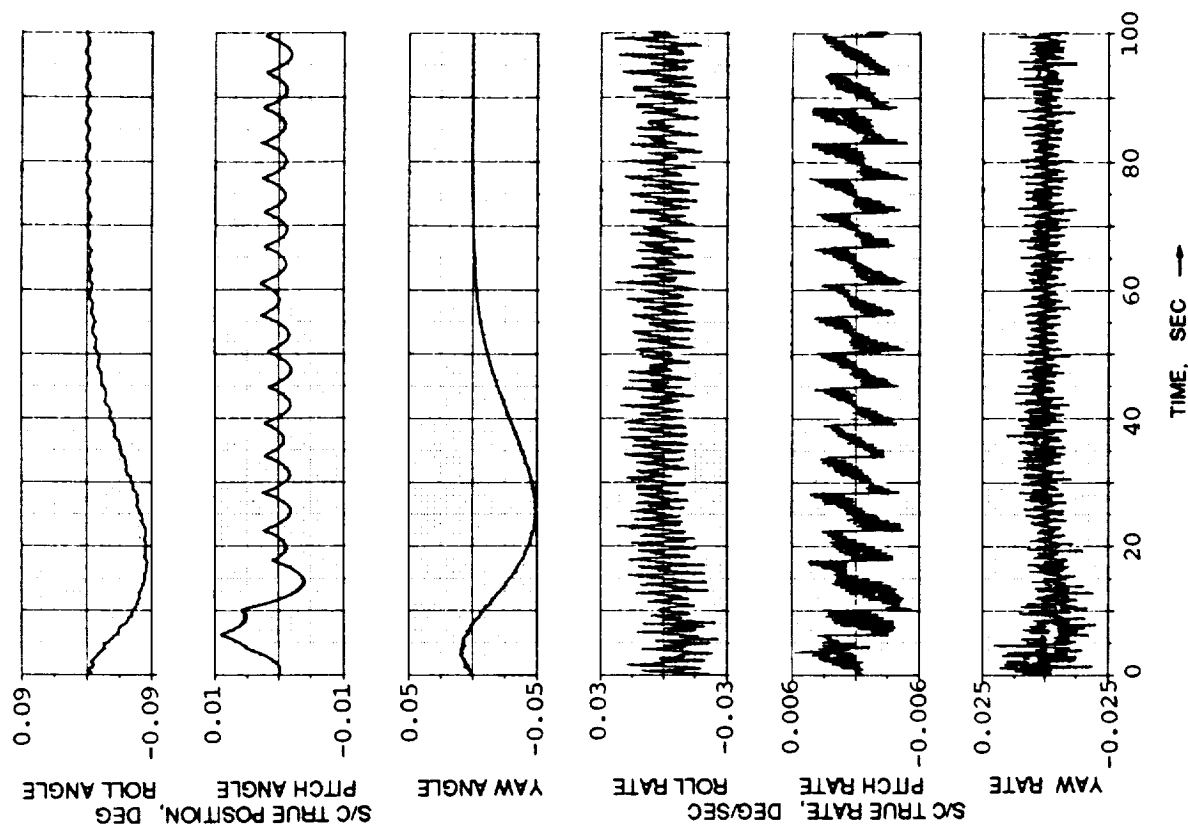


Figure 7.3 Stationkeeping Mode Control Performance From A 100 -sec South Maneuver with Zero Initial Acceleration Bias Estimates - 100% Modal Frequency Increase, 0.25% Structural Damping

8. Concluding Remarks

The design and analysis of a stationkeeping control system for a body-stabilized spacecraft having flexible solar wings of 3 solar panels per wing were presented. The use of the hybrid coordinate modeling approach along with frequency domain analysis technique accurately modeled the rigid-flex coupling behavior. The design philosophy to stabilize the structural modes and to smooth the flexure was discussed. The control system was designed to gain and/or phase-stabilize the structural modes. The lead inherent rate gyro references, the structural filters and the time-varying bias estimation gains were key factors to achieve a successful design. Control performance of Stationkeeping/Transition Modes during a south maneuver under the worst case simulation environment was demonstrated through digital simulation. The accuracy of the analytical model for structural mode/control loop interaction is best verified with the test data obtained from comprehensive ground testing. The control system as presented allows for a high degree of uncertainty on mode shape and frequency.

An alternate, indirect implementation of flexible vehicle dynamics has been presented. The effort required to derive and to implement the equations of motion can be significantly reduced. A formulation through the virtual work principle allowed consistent derivation and discretization of the flexible domain within the context of the finite element method. Extensions into nonlinear flexible models can be made.

Acknowledgement - A portion of this work supported by the C. S. Draper Laboratory Internal Research & Development is gratefully acknowledged.

References

1. P.C. Hughes, *Spacecraft Attitude Dynamics*, John Wiley & Sons (1986).
2. P.W. Likins, "Analytical Dynamics and Nonrigid Spacecraft Simulations", *Technical Report 32-1593*, Jet Propulsion Laboratory, Pasadena, CA (1974).
3. P.W. Likins and G.E. Fleischer, "Results of Flexible Spacecraft Attitude Control Studies Utilizing Hybrid Coordinates", *Journal of Spacecraft and Rockets*, Vol. 8, 264-273 (1971).
4. J. Storch and S. Gates, "Equations of Motion for a Flexible Spacecraft - Lumped Parameter Idealization", *Technical Report CSDL-R-1582*, C.S. Draper Laboratory, Cambridge, MA (1982).
5. S. Gates and D.S. Kang, "An Attitude Dynamics Model of the Hughes HS-601 Spacecraft", *Technical Report CSDL-R-2156*, C.S. Draper Laboratory, Cambridge, MA (1989).
6. *SD/FAST User's Manual, Version 88/02/20*, Symbolic Dynamics, Inc., Mountain View, CA (1988).
7. D.E. Rosenthal and M.A. Sherman, "High Performance Multibody Simulations via Symbolic Equation Manipulation and Kane's Method", *Journal of the Astronautical Sciences*, Vol. 34, No. 3, 223-239 (1986).
8. D.B. Schaechter, D.A. Levinson, T.R. Kane, *AUTOLEV User's Manual*, OnLine Dynamics, Inc., Sunnyvale, CA (1988).
9. M. Sayers, *AUTOSIM User's Manual, Version 1.0 B8*, Univ. of Michigan, Transportation Research Institute, Ann Arbor, MI (1990).
10. B. Wie and C.T. Plescia, "Attitude Stabilization of Flexible Spacecraft During Stationkeeping Maneuvers", *Journal of Guidance and Control, AIAA* (1983).
11. A.N. Panchuk and P.D. Hattis, "A Frequency Domain Stability Analysis of a Phase Plane Control System", *J.Guidance*, Vol. 8, No. 1 (1985).
12. J.F. Yocum and L.I. Slafer, "Control System Design in the Presence of Severe Structural Dynamics Interactions", *J.Guidance*, Vol. 1, 109-116 (1978).
13. L.I. Slafer, "In-Orbit Evaluation of the Control System/Structural Mode Interactions of the OSO-8 Spacecraft", *Dynamics and Control of Large Flexible Spacecraft Proceedings of the Second VPI&AIAA Symposium*, June 21-23, 111-127 (1979).
14. D.S. Kang, "Present Finite Element Technology from a Hybrid Formulation Perspective", *Computers and Structures*, 35, 321-327 (1990).